

# Global scale error assessments of soil moisture estimates from microwave-based active and passive satellites and land surface models over forest and mixed irrigated/dryland agriculture regions



Hyunglok Kim<sup>a,b,\*</sup>, Jean-Pierre Wigneron<sup>c</sup>, Sujay Kumar<sup>d</sup>, Jianzhi Dong<sup>e</sup>, Wolfgang Wagner<sup>f</sup>, Michael H. Cosh<sup>e</sup>, David D. Bosch<sup>g</sup>, Chandra Holifield Collins<sup>h</sup>, Patrick J. Starks<sup>i</sup>, Mark Seyfried<sup>j</sup>, Venkataraman Lakshmi<sup>a</sup>

<sup>a</sup> The Department of Engineering Systems and Environment, University of Virginia, Charlottesville, VA 22904, USA

<sup>b</sup> School of Data Science, University of Virginia, Charlottesville, VA 22904, USA

<sup>c</sup> Interactions Sol Plante Atmosphère (ISPA), Unité Mixte de Recherche 1391, Institut National de la Recherche Agronomique (INRAE), CS 20032, 33882 Villenave d'Ornon CEDEX, France

<sup>d</sup> Hydrological Sciences Laboratory, NASA GSFC, Greenbelt, MD 20771, USA

<sup>e</sup> Hydrology and Remote Sensing Laboratory, USDA-ARS, Beltsville, MD 20705, USA

<sup>f</sup> Department of Geodesy and Geoinformation, TU Wien, 1040 Vienna, Austria.

<sup>g</sup> Southeast Experimental Watershed Research Laboratory, USDA-ARS, Tifton, GA, USA.

<sup>h</sup> Southwest Watershed Research Center, USDA-ARS, Tucson, AZ, USA.

<sup>i</sup> Grazinglands Research Laboratory, USDA-ARS, El Reno, OK, USA.

<sup>j</sup> Northwest Watershed Research Center, USDA-ARS, Boise, ID, USA.

## ARTICLE INFO

### Keywords:

Soil moisture  
Satellite-based soil moisture data  
Land surface model  
ASCAT  
SMOS  
AMSR2  
SMAP  
ERA5  
GLDAS  
Triple collocation analysis  
In-situ soil moisture

## ABSTRACT

Over the past four decades, satellite systems and land surface models have been used to estimate global-scale surface soil moisture (SSM). However, in areas such as densely vegetated and irrigated regions, obtaining accurate SSM remains challenging. Before using satellite and model-based SSM estimates over these areas, we should understand the accuracy and error characteristics of various SSM products. Thus, this study aimed to compare the error characteristics of global-scale SSM over vegetated and irrigated areas as obtained from active and passive satellites and model-based data: Advanced Scatterometer (ASCAT), Soil Moisture and Ocean Salinity (SMOS), Advanced Microwave Scanning Radiometer 2 (AMSR2), Soil Moisture Active Passive (SMAP), European Centre for Medium-Range Weather Forecasts Reanalysis 5 (ERA5), and Global Land Data Assimilation System (GLDAS). We employed triple collocation analysis (TCA) and calculated conventional error metrics from in-situ SSM measurements. We also considered all possible triplets from 6 different products and showed the viability of considering the standard deviation of TCA-based numbers in producing robust results.

Over forested areas, it was expected that model-based SSM data might provide more accurate SSM estimates than satellites due to the intrinsic limitations of microwave-based systems. Alternately, over irrigated regions, observation-based SSM data were expected to be more accurate than model-based products because land surface models (LSMs) cannot capture irrigation signals caused by human activities. Contrary to these expectations, satellite-based SSM estimates from ASCAT, SMAP, and SMOS showed fewer errors than ERA5 and GLDAS SSM products over vegetated conditions. Furthermore, over irrigated areas, ASCAT, SMOS, and SMAP outperformed other SSM products; however, model-based data from ERA5 and GLDAS outperformed AMSR2. Our results emphasize that, over irrigated areas, considering satellite-based SSM data as alternatives to model-based SSM data sometimes produces misleading results; and considering model-based data as alternatives to satellite-based SSM data in forested areas can also sometimes be misleading. In addition, we discovered that no products showed much degradation in TCA-based errors under different vegetated conditions, while different irrigation conditions impacted both satellite and model-based SSM data sets.

The present research demonstrates that limitations in satellite and modeled SSM data can be overcome in

\* Corresponding author at: The Department of Engineering Systems and Environment, University of Virginia, Charlottesville, VA 22904, USA.  
E-mail address: [hk5kp@virginia.edu](mailto:hk5kp@virginia.edu) (H. Kim).

many areas through the synergistic use of satellite and model-based SSM products, excluding areas where satellite-based data are masked out. In fact, when four satellite and model data sets are used selectively, the probability of obtaining SSM with stronger signal than noise can be close to 100%.

## 1. Introduction

Evapotranspiration (ET) over forest areas is a significant contributor to total global precipitation (Cox et al., 2000; Ding et al., 2011). One of the most important hydrological variables in controlling the variability of ET is soil moisture (SM) on the surface and in the root zone (Juárez et al., 2007) since SM in the deep soil layer permits a relatively high ET rate throughout the year. In addition, under sufficient SM conditions, the variability of ET is controlled by net radiation, vapor pressure deficit, and wind speed (Costa et al., 2004; Werth and Avissar, 2004).

The variability of 5-cm SM can be closely coupled with root-zone (0–100 cm) soil moisture (RZSM) variability. Therefore, an accurate estimation of surface SM (SSM) allows more precise prediction of RZSM as surface wetness influences infiltration to the deeper layers and consequently allows for improved modeling of the root zone and the plant's available water at a coarse-scale spatial resolution. Much previous research has shown that using SSM data obtained by satellite can significantly improve the prediction of RZSM (Das and Mohanty, 2006; Ford et al., 2014). Specifically, RZSM can be effectively predicted with an exponential decay filter, as shown in Wagner et al. (1999). Furthermore, Das and Mohanty, (2006) and Dumedah et al. (2015) showed that assimilating remotely-sensed SSM data into land surface models (LSM) provides improved SM quality with consistent accuracy at both the surface and root zone layers. More recently, Reichle et al. (2017) introduced a Level-4 surface (0–5 cm) and RZSM product generated by assimilating brightness temperature (Tb) obtained from the Soil Moisture Active Passive (SMAP) into an LSM. Their product showed significant improvement in the performance of RZSM after assimilation of SMAP Tb data. All these studies support the fact that SSM obtained by remotely-sensed methods can greatly benefit the prediction of RZSM. However, SM from deeper layers down to several meters would be hard to directly observe from L-band microwave products. One promising method for predicting SM deeper than 5 cm from space is the use of P-band Synthetic Aperture Radar (SAR) data (Chapin et al., 2012).

All these factors indicate that knowing the variability of SSM and obtaining accurate SSM is important in understanding land-atmosphere interactions. Here, we conducted a global analysis with a more specific focus on forested ecosystems and irrigated lands as they represent areas where both remote sensing retrievals and model predictions may have some limitations.

In forest, ground-based observation methods are limited spatially and heterogeneity of the landsurface increases the uncertainty of any ground based SSM estimates. It has also been demonstrated that over dense forest areas such as the Amazon River Basin and Southeast Asia, the accuracy of SSM retrievals from microwave sensors may be limited (Al-Yaari et al., 2014a; Burgin et al., 2017). Over densely vegetated areas, most of the satellite-based data is usually masked out because plant biomass saturates the microwave signal, resulting in high data errors and uncertainties.

Irrigated fields are artificial ecosystems that are created and managed by human beings. Anthropogenic techniques directly impact the distribution of SM across the topsoil layer (Cho et al., 2019; Lawston et al., 2017; Seneviratne et al., 2010). These effects, in turn, alter soil characteristics such as surface-layer soil macroporosity, infiltration and percolation rates, discharge fluxes, and evaporative demands. Several studies have shown that irrigation plays a critical role in increasing ET, and that it directly impacts local surface energy and water budget partitioning (Cook et al., 2011; Crow et al., 2005; Lobell et al., 2009; Sacks et al., 2009). Consequently, irrigation affects the large-scale

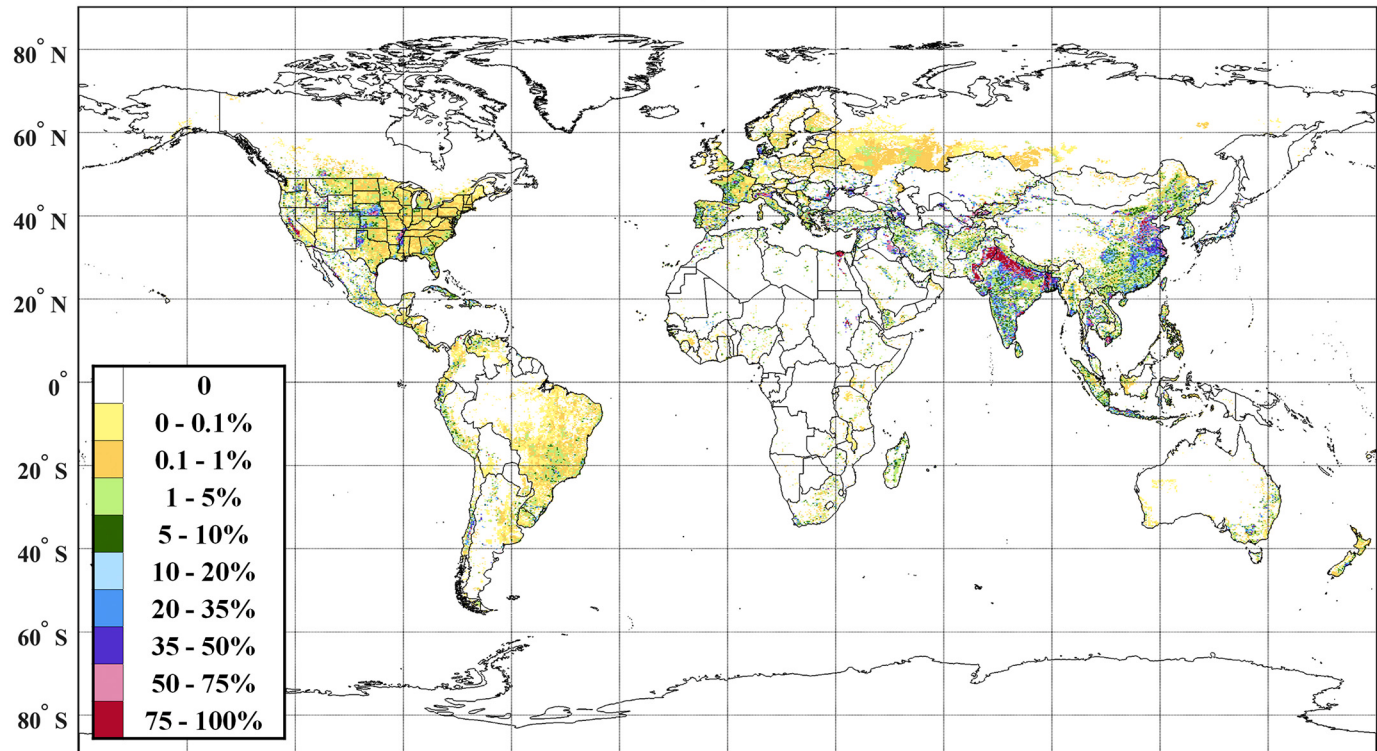
volumetric atmospheric thermodynamic features from the lower atmosphere to the upper troposphere, thus altering the entire global-scale water cycle (Pei et al., 2016; Puma and Cook, 2010); and human activities specially designed to produce crops more rapidly will affect SM conditions and significantly impact natural biosphere-atmosphere interactions (Lo and Famiglietti, 2013).

Specifically, the size of a single unit of the center-pivot irrigation system or a linear/lateral move irrigation machine is less than 1 km, but irrigation conducted using these systems are usually clustered with several center pivot circles and lines. Thus, the scale of the irrigation area can be greater than 25 km, meaning it can be seen from space via optical and infrared sensors (Deines et al., 2017). Many attempts have been made to compare SSM simulations from several different land surface models against satellite SSM products in order to identify irrigated areas and improve the quality of SSM in LSMs (Abolafia-Rosenzweig et al., 2019; Deines et al., 2017; Escorihuela and Quintana-Seguí, 2016; Kumar et al., 2015; Lawston et al., 2017). These studies have found SSM data obtained from space to be extremely useful in detecting irrigation activities and improving the SM estimation in LSMs. However, few studies have evaluated and intercompared satellite- and model-based SSM data over irrigated areas even though SM information over irrigated areas is critical in developing coupled accurate land-atmosphere models (Al-Yaari et al., 2019a). Furthermore, it should also be noted that in-situ sensors are rarely available for irrigation in agricultural lands; thus, it is important to utilize remotely sensed data that can estimate SSM variability over irrigated areas.

To fully understand the role of forests and the effects of irrigation on Earth's environment and hydrological cycle, near-real-time large-scale SM data sets can be very useful (Lawston et al., 2017); therefore, it is necessary to employ satellite- and/or model-based SSM products. Currently, hydrologists track changes in SSM levels using global-scale SSM estimates retrieved from active and passive microwave remote sensing, and LSMs (Karthikeyan et al., 2017; Kumar et al., 2006; Rodell et al., 2004). This provides an effective method for monitoring near-real-time SSM contents at various temporal and spatial resolutions. Researchers have proposed various methods of obtaining near-surface SM retrievals from satellite microwave instruments (Bindlish et al., 2015; Entekhabi et al., 2010; Jackson et al., 2010; Kerr et al., 2001; Lakshmi et al., 1997; Wagner et al., 1999; Wigneron et al., 2017). In addition to the active and passive satellite-based microwave SM missions, including the Advanced Microwave Scanning Radiometer (AMSR-E), the Advanced Scatterometer (ASCAT), the Soil Moisture and Ocean Salinity (SMOS), the Advanced Microwave Scanning Radiometer 2 (AMSR2), and the SMAP mission, researchers have also experimented applying Global Navigation Satellite System (GNSS) signals to the investigation of SSM (Kim and Lakshmi, 2018). The primary advantage of using satellite-based SSM data is that they are derived from observation-based (i.e., non-artificial) SSM retrieval systems; thus, they have a strong potential to detect SSM variation caused by human activities such as irrigation (Lawston et al., 2017). Model-produced SSM data cannot detect such changes because the major forcing element used to predict SSM values is precipitation, and models cannot distinguish between natural and anthropogenic effects that occur over land since they cannot easily evaluate the amount of irrigated water.

One of the major drawbacks in using current satellite-based SSM data based on microwave retrieval systems is the limitation caused by revisiting time: satellites cannot provide spatially and temporally continuous coverage due to their sun-synchronous orbits. They can only provide SSM estimates one to two times per day, hampering researchers who are attempting to describe the fundamental processes that control

**(a) Area Equipped for Irrigation (AEI) in Percentage of Land Area from GMIA**



**(b) Yearly Vegetation Optical Depth (VOD)**

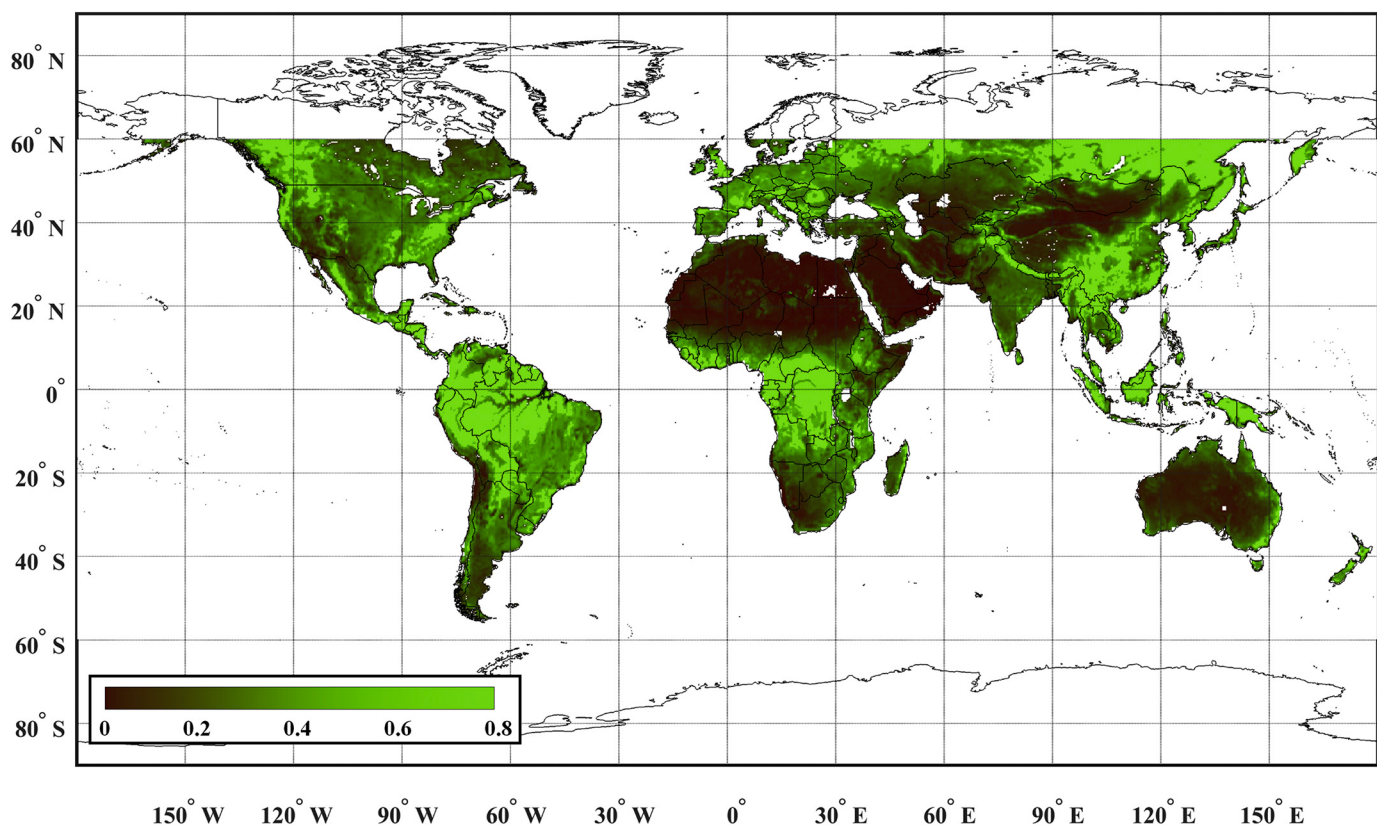


Fig. 1. Maps of (a) areas equipped for irrigation (AEI) and (b) X-band vegetation optical depth (VOD) (2015–2019).

the terrestrial hydrologic cycle (Kim and Lakshmi, 2019). It has also been investigated that over dry areas such as the Sahara and Taklamakan deserts, the accuracy of SSM retrievals from microwave sensors may be limited (Al-Yaari et al., 2014a; Burgin et al., 2017). Over densely vegetated areas, most of the data is usually masked out because plant biomass saturates the microwave signal, resulting in high data errors and uncertainties. Over dry areas, the challenges are caused by problems in estimating the thickness of the emitting layer and the effective temperature. Low-frequency microwaves (i.e., L-bands) penetrate dry soils more deeply, so the signals are representative of deeper soil layers. Signals from deep soil layers can cause problems for active systems (e.g., radar; ASCAT). The reason is that radar signals provide highly directional measurements and are thus more sensitive to the roughness of sub-surface scatterers (e.g., rock below a layer of dry sand) (Ulaby et al., 2014; Morrison and Wagner, 2019; Wagner et al., 2013). Problems similar to those of ASCAT are also seen in SMOS, SMAP, and AMSR2 data, although the effects appear to be much smaller.

By contrast to satellite-based SSM estimates, model-based SSM data are more flexible in terms of temporal and spatial coverage, and they can provide SM estimates of various depths (Rodell et al., 2004). LSMs are forced with various observation sources, including satellite data, precipitation observations from gauges and radar, and output from numerical prediction models. The necessary models' land parameters are calculated from existing high-resolution vegetation and soil coverage as constant values (e.g., soil texture, land use land cover information, etc.). With these input data sets, it is possible to predict SM values over densely vegetated areas from LSMs that are limited in regions for which microwave-based SM retrievals may be used. However, model-based SM data are far from perfect simulations of hydrological variables; they are mere simplifications of the real world. Thus, modeled results might not effectively reflect near-real-time changes in earth surfaces, including fluxes (e.g., evaporation and runoff), storage (e.g., SM or snow), and real-time land surface changes (e.g., wildfires). Consequently, modeled results are limited in their ability to detect anthropogenic activities (e.g., irrigation and biomass burning) and natural phenomena (e.g., wildfires and dust outbreaks). It is apparent, then, that we should avoid relying too much on one source of SSM information and try to utilize SSM data from multiple sources over the forest and irrigated areas.

Acknowledging the existence of these limitations in satellite- and model-based SM data sets, the present study will focus on the error characteristics of both satellite-based and global-scale models' SSM estimates over the forest and irrigated areas. For this analysis, we will focus on using a triple collocation analysis (TCA) to inter-compare the global-scale error patterns of four satellite-based SSM data sets obtained from the forest and irrigated regions by ASCAT, SMOS, AMSR2, and SMAP; and two model data sets from the European Centre for Medium-Range Weather Forecasts Reanalysis 5 (ERA5) and NASA's GLDAS.

TCA has been used in several studies to evaluate global-scale remotely sensed and model-based SSM data (Crow et al., 2005; Dong and Crow, 2017; Draper et al., 2013; Gruber et al., 2016; McColl et al., 2014; Miyaoka et al., 2017; Scipal et al., 2010; Stoffelen, 1998; Su et al., 2014a, 2014b). In recent years, especially, its use in evaluating SMAP SSM data has significantly enhanced our understanding of the absolute and relative error characteristics of satellite-based SSM estimations (Chen et al., 2017, 2018; Cho et al., 2015; Dong et al., 2018; Yilmaz and Crow, 2014). TCA has been used to intercompare SMAP and other satellite-based SSM products and it has also provided information critical to the application of satellite-based SM data in such research fields as the assimilation of satellite-based SSM data into LSMs and merging SSM from various satellite sensors (Gruber et al., 2017).

One of the most important tasks in conducting TCA is deliberately composing triplets to avoid the violation of TCA assumptions (Dong and Crow, 2018; McColl et al., 2014). In particular, the assumption about the statistical nature of errors, including mutual independence, the validity of assuming that the different data sets represent the same

physical variables, orthogonality to the truth value, etc., are required for robust TCA. However, conformity to all recognized TCA assumptions is close to impossible with current satellite and model-based SSM data due to various limitations (e.g., different representative depth of each data set and similar retrieval algorithms; further details are included in the methodology section). This fact indicates that considering a single triplet for TCA would lead to biased results; however, many previous studies have estimated satellite-based data sets (e.g., SSM, ET, precipitation, surface albedo, and wind vector components) with a single triplet mostly because there were not enough data sets for building alternative triplet (Alemohammad et al., 2015; Caires, 2003; Khan et al., 2018; Kim et al., 2018; Miyaoka et al., 2017; Wu et al., 2019).

In the present research, we considered all possible triplets from four satellites and two model-based SM products. The main goal of this research was to compare and estimate the error patterns of current satellite and LSM systems over forest and irrigated areas, which have been considered the most challenging environmental conditions for SSM estimations by both satellite and LSMs. For the girdcell-scale information of irrigation activities and density of the vegetation matter, we used the Global-scale Irrigation Data (GMIA; Section 2.1) and Vegetation Optical Depth (VOD; Section 2.2), respectively. We have also illustrated the lowest possible errors that can be obtained from selective uses of up-to-date satellite and model-based SSM products on a global scale.

## 2. Data sets

### 2.1. The global-scale irrigation data

In the present study, we assumed that the Global Map of Irrigation Areas (GMIA) reasonably represent areas of irrigation (Siebert et al., 2013). By combining sub-national and national-level statistics with geospatial information, Siebert et al. (2005) derived the percentage of area equipped for irrigation (AEI) at a spatial resolution of 5 min. Hence, the data used in this study from the GMIA map estimates the areas of land equipped for irrigation as a percentage of the total area on a raster of 10 classes of irrigated areas (Fig. 1(a)). The GMIA data is widely utilized for various purposes; for instance, it is used as reference data (e.g., the ground-truth data of irrigation areas) to validate newly developed irrigation maps (Salmon et al., 2015; Thenkabail et al., 2009; Zohaib et al., 2019), and it is utilized to predict the impact of irrigation activities on global climate systems (Pryor et al., 2016; Tuinenburg and de Vries, 2017). Based on the empirical cumulative distribution function,  $F(\text{AEI})$ , we defined barely, moderately, and actively irrigated regions: barely irrigated regions were defined as those in which the AEI was less than 0.8% ( $F^{-1}(1/3)$ ), moderately irrigated regions were defined as those in which the AEI was greater than 0.80% but less than 12.78% ( $F^{-1}(2/3)$ ), and actively irrigated regions were defined as those in which the AEI was greater than 12.78%. In addition, in order to consider cropland areas alone, we used the cropland areas extracted from the land classification map from the International Geosphere-Biosphere Programme (IGBP) (Section 2.5).

### 2.2. Vegetation optical depth

Vegetation Optical Depth (VOD) can provide useful information regarding the water content of vegetation and the structure of above-ground vegetation (Konings et al., 2017). In this study, we employed the LPRM-based yearly-averaged VOD computed at X-band which was calculated from data obtained during the AMSR2 descending overpass. This product was retrieved from the AMSR2 brightness temperature measurements using the Microwave Polarization Difference Index (Owe et al., 2001). We used VOD data from AMSR2 as X-band is less vulnerable to radio frequency interference (RFI). Based on the empirical cumulative distribution function,  $F(\text{VOD})$ , we defined sparsely, moderately, and densely forested regions:

sparserly vegetated regions were defined as those in which the VOD was less than 0.31 ( $F^{-1}(1/3)$ ), moderately vegetated regions were defined as those in which the VOD was greater than 0.31 but less than 0.62 ( $F^{-1}(2/3)$ ), and densely forested regions were defined as those in which the VOD was greater than 0.62. Fig. 1(b) shows the average VOD value during the study period (from 2015 to 2019). In addition, in order to mask out deserts, semi-deserts, urban and built-up areas, and irrigated crop areas, we used the land classification map from the AEI and IGBP data sets (Fig. 1(a) and Section 2.5).

### 2.3. Satellite soil moisture data

#### 2.3.1. Advanced Scatterometer (ASCAT)

The ASCAT sensors are onboard the Meteorological Operational A, B, and C (MetOp-A (October 2006), MetOp-B (September 2012), and MetOp-C (November 2018)) satellites (Wagner et al., 2013) which are

operated by European organization for the exploitation of METeorological SATellites (EUMETSAT). ASCAT includes an active microwave remote-sensing instruments and it acquires radar backscatter measurements at a frequency of C-band (5.3 GHz, wavelength = 5.7 cm). The ASCAT overpasses at 09:30 and 21:30 local time in descending and ascending orbit, respectively. The degree of saturation is calculated from the backscattering coefficient measured at a reference angle of 40° based on the method of Wagner et al. (1999), by using the historically lowest (dry, 0%) and highest (wet, 100%) observed backscatter. The volumetric SSM content given in  $\text{cm}^3 \text{cm}^{-3}$  was produced by multiplication with the soil porosity data (Wagner et al., 2013). In this study, we used ASCAT SSM data distributed by the EUMETSAT H-SAF called H111, which is based on the TU Wien algorithm. H111 is a combination of MetOp-A and B satellites. This product includes a 12.5 km spatial sampling, and temporal resolution depends on the latitudinal location and number of MetOp satellites it uses. A daily sampling can be

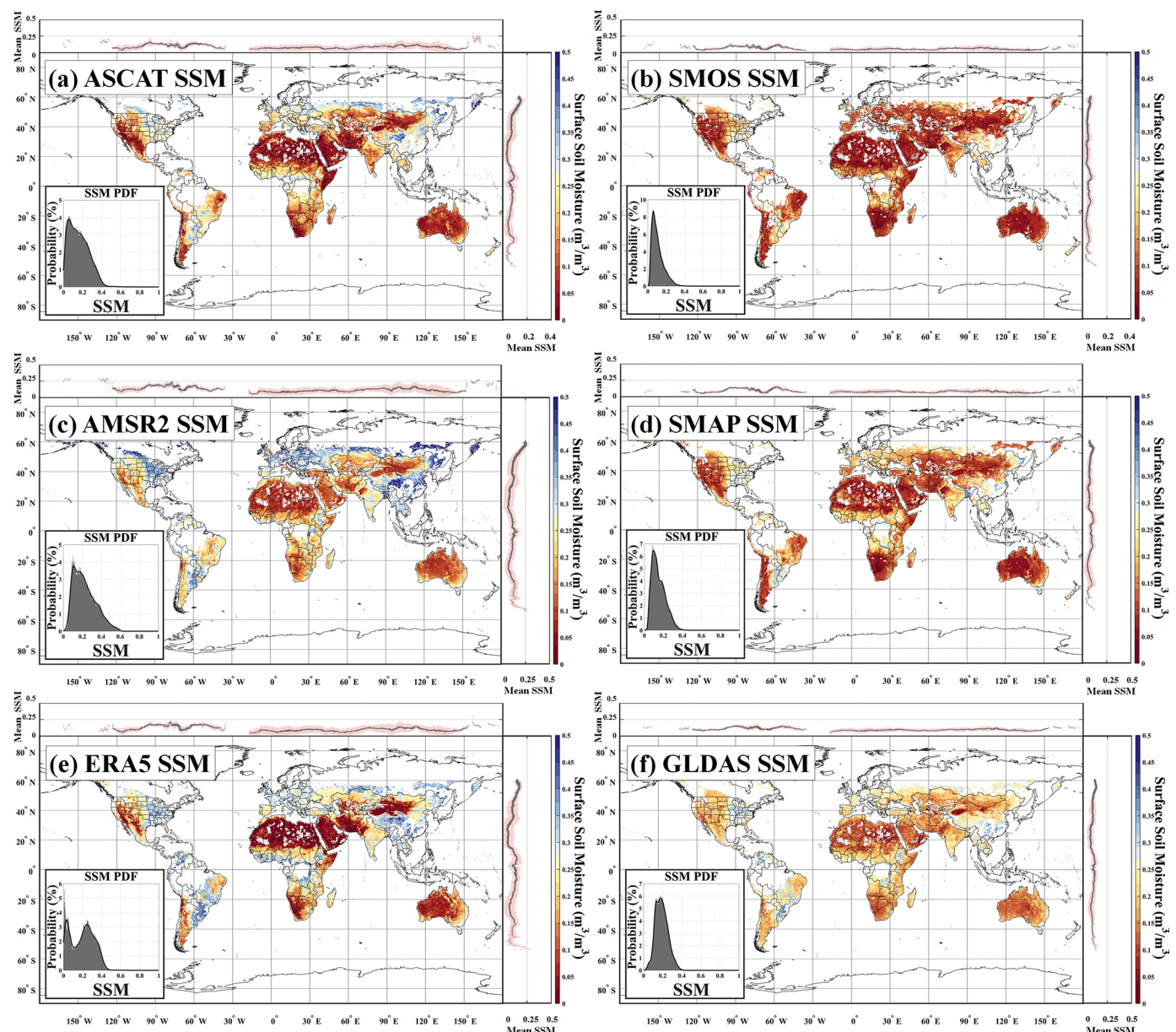


**Fig. 2.** Maps of averaged (from 2015 to 2019) surface soil moisture (SSM) for (a) ASCAT, (b) SMOS, (c) AMSR2, (d) SMAP, (e) ERA5, and (f) GLDAS. Average values were calculated over the pixel where all the six SSM data are available both in space and time. Upper and right panels indicate longitude and latitude zonal means of SSM, respectively. Inset graphs represent PDF for each data set, marker sizes in zonal plots illustrate proportional to zonal land area, and the shaded region shows ± 1 standard deviation.

obtained using only MetOp-A, and two observations per day can be achieved by using both MetOp satellites near the mid-latitudes (Brocca et al., 2019). The average of ASCAT SSM data from 2015 to 2019 is shown in Fig. 2(a).

### 2.3.2. Soil moisture and ocean salinity (SMOS)

The SMOS satellite is one of the European Space Agency (ESA)'s Earth Explorer missions, launched in November 2009. SMOS carries Microwave Imaging Radiometer with Aperture Synthesis (MIRAS) and estimates the SSM conditions as well as the salinity of seawater. The MIRAS instrument is an L-band (1.41 GHz, wavelength = 21 cm) 2-D interferometric radiometer and it observes the variations in the natural microwave emitted from the surface of the earth's surface with multiple incidence angles (0°–65°). The SMOS mission's accuracy requirement is 0.04 cm<sup>3</sup>cm<sup>-3</sup> at a depth of 3–5 cm SSM at 35–50 km spatial resolution every 2–3 days (Kerr et al., 2001). The SMOS overpasses at 18:00 and 06:00 local time in descending and ascending orbit, respectively. Most recently, the SMOS-IC product has been developed (Fernandez-Moran et al., 2017). This product is considered to produce high-quality SMOS SSM (Al-Yaari et al., 2019b; Li et al., 2020; Ma et al., 2019), and SMOS-IC is available from 2009 to 2019. In this study, we used SMOS-IC SSM V106 data (hereafter SMOS) and considered scene flag information. The data was used if the scene flag was greater than one. This allowed us to remove topography effects, pollution (i.e., the water, urban area, or ice mixture was greater than 10% of the pixel), and frozen pixels (i.e., the ECMWF surface temperature was lower than 273 K). Tb-RMSE flag values larger than 8 K were masked out to avoid areas that showed a strong RFI effect on SSM data. The SSM range from 0 m<sup>3</sup>/m<sup>3</sup> to 0.6 m<sup>3</sup>/m<sup>3</sup> was used (Li et al., 2020). Filtering SMOS-IC data based on these quality flags allowed us to use the highest quality SSM estimates. The annual average of SMOS SSM data from 2015 to 2019 is shown in Fig. 2(b).

### 2.3.3. Advanced microwave scanning radiometer 2 (AMSR2)

Through the collaboration of NASA and JAXA, the AMSR2 sensor onboard the Global Change Observation Mission 1-Water (GCOM-W1) platform was launched on May 2012 as the successor to JAXA'S Advanced Microwave Scanning Radiometer for Earth Observing System (AMSR-E) sensor which terminated operation in October 2011 (Bindlish et al., 2018). AMSR2 has 7 frequencies and 14 channels, and for the SSM estimation, AMSR2 uses three different microwave frequency bands at C1 (6.9 GHz, wavelength = 4.3 cm), C2 (7.3 GHz, wavelength = 4.1 cm), and X (10.6 GHz, wavelength = 2.8 cm), with a 1450 km swath-width. Its incidence angle is fixed at 55°. Their original ground resolutions depend on frequency channels (C1-band: 24 × 42 km, C2-band: 34 × 58 km; X-band: 35 × 62 km) with a revisit time of 1–2 days and it crosses the equator at 01:30 local times and 13:30 local time in descending and ascending orbits, respectively (Bindlish et al., 2018). In this study, we used X-band the Land Parameter Retrieval Model (LPRM) AMSR2 data (descending path). We selected X-band based LPRM SSM product because SSM from the C-band wavelength might have partially correlated errors with other satellite-based SSM products (please refer to Section 3.2 for detailed information). The annual average of AMSR2 SSM data from 2015 to 2019 is shown in Fig. 2(c).

### 2.3.4. Soil moisture active passive (SMAP)

The SMAP mission is the Earth observation satellite developed by NASA in response to the National Research Council's Earth Science Decadal Survey. The mission was launched in January 2015 and began regular data collection in April of 2015 (Entekhabi et al., 2010). SMAP provides estimates of the moisture content of the top 0–5 cm soil layer with a revisit every 1–3 day in a near-polar and sun-synchronous orbit, and it overpasses the Equator at approximately 06:00 and 18:00 local time in descending and ascending orbits, respectively. Similar to the SMOS SSM retrieval system, SMAP also observes the variations in the

natural microwave emitted from the surface of the earth surface provided by a low microwave frequency L-band radiometer (1.41 GHz, wavelength = 21 cm) with nominal incidence angle 40° (O'Neill et al., 2015). In the present study, we used the Level-3 SMAP SSM data from the descending overpass time observations, the data were masked for SSM lower than 0.02 cm<sup>3</sup>cm<sup>-3</sup> and higher than 0.50 cm<sup>3</sup>cm<sup>-3</sup>, and the retrieval information in the retrieval quality flag showed recommended quality (0 Bit). Level-3 radiometer global daily 36 km retrievals in Equal-Area Scalable Earth 2 (EASE2) grid are the composition of SMAP Level-2 SSM retrievals. We used SMAP L3 Version 6 which is the baseline algorithm is Single Channel Algorithm-Vertical (SCA-V) (<https://nsidc.org/data/SPL3SMP VERSIONS/6>). The annual average of SMAP SSM data from 2015 to 2019 is shown in Fig. 2(d).

## 2.4. Model-based data

### 2.4.1. European Centre for Medium-Range Weather Forecasts Reanalysis 5 (ERA5)

The ERA5 data, available from 1979 to present, is produced by ECMWF and is available from the Copernicus Climate Change service. ERA5 is currently the latest global climate reanalysis data produced by ECMWF and follows other reanalysis products: the First Global Atmospheric Research Program, Global Experiment, the ECMWF Reanalysis 15, the ECMWF Reanalysis 40, and the ERA-Interim. The ERA5 products are expected to be updated once per month, with a delay of 2 months for quality assurance and for correcting technical problems with production. The forcing data is obtained by assimilating observation data (e.g., 2-m temperature and ASCAT SSM) through a 4D-VAR data assimilation system and a simplified extended Kalman filter, respectively. This forcing data is derived from the ERA5-Land single simulation without coupling to the atmospheric module of the ECMWF's Integrated Forecasting System (IFS) or to the ocean wave model of the IFS. ERA5 has been providing spatially complete and gridded atmospheric and land surface variables with an hourly temporal resolution and a spatial resolution from 0.1° × 0.1° (9 km) from January 2001 to present. SSM and surface temperature are provided as instantaneous parameters that represent time scales equal to the model time step. In the present study, we used ERA5 top 0–7 cm SSM data along with the satellite data sets for TCA and surface temperature data in order to exclude SSM data when the temperature was lower than 273.13 K. The annual average of ERA5 SSM data from 2015 to 2019 is shown in Fig. 2(e).

### 2.4.2. Global land data assimilation system (GLDAS)

GLDAS data is produced by the Land Information System (LIS) software framework (Kumar et al., 2006). The GLDAS Version 2 has two components: one forced with the Princeton meteorological forcing data (from 1948 to 2010; GLDAS 2.0), and the other forced with a combination of model and observation-based forcing data sets (from 2010 to present; GLDAS 2.1). In this study, we used the GLDAS 2.1-Noah (hereafter GLDAS) that is based on a combination of model and various satellite- and ground-based observations. It produces the best estimation of the land surface conditions simulated with the Noah Model 3.3 in LIS Version 7 (Rodell et al., 2004). GLDAS data provides numerous atmospheric and land surface variables with a temporal resolution of 3-hourly and monthly with a spatial resolution from 0.25° × 0.25° to 1° × 1°. In the present study, we performed TCA using the top 0–10 cm of GLDAS SSM data together with a satellite data sets and surface temperature data (with 0.25° × 0.25° spatial resolution); we only used SSM data where the surface temperature was over 273.15 K. The annual average of GLDAS SSM data from 2015 to 2019 is shown in Fig. 2(f).

## 2.5. Ground soil moisture observations

To evaluate the four remotely sensed and two model products, and to compare the conventional error metrics with the TCA-based error

metrics, we employed SM data obtained from both dense and sparse networks. For the sparse SM stations, we downloaded data from the International Soil Moisture Network (ISMN). ISMN is a web-based data center that collects and organizes ground-based SM measurements, and the data is freely available through a web interface (<https://ismn.geo.tuwien.ac.at/>; accessed on 1. June. 2020). The ISMN in-situ SM data have been widely used to validate different satellite-based SSM retrievals and land surface models, and the ISMN currently holds ground-based SM measurements provided by more than 2000 ground stations which are operated by more than 55 different networks (Dorigo et al., 2011, 2013, 2015). In this study, we used ISMN SM stations that measure SM at a depth of less than 10 cm and provide data which covers the study period (2015–2019). In total, 1662 ground-based, sparse-SM stations were tested based on the quantity and quality of their SM data (black circles in Fig. 3). All data sets were quality controlled (Dorigo et al., 2013) and cross screened in order to narrow the data to grid pixels for which all six satellite- and model-based SM data sets were commonly attainable. In order to obtain robust statistical results, we excluded SM stations for which the corresponding grid pixel had < 300 data points in time. As a further step, if multiple stations were situated within the same grid pixel, we arithmetically averaged all the stations' SM values. After preprocessing, data at 180 sites were viable; most of these were located in the contiguous United States (CONUS) and European countries (red filled circle in Fig. 3). A detailed description of the ISMN used in this study is summarized in Table S1.

In addition to the sparse networks, we also considered dense SM networks in calculating relative error metrics (please refer to Section 4.2 for a detailed discussion about our use of dense and sparse networks). For dense ground-based SM observations, we used five networks among the SMAP core validation sites (Colliander et al., 2017). For the watershed networks, we used SM data managed by the United States Department of Agriculture Agricultural Research Service (ARS), selecting data for the study period (2015–2019). The networks chosen were Walnut Gulch (WG; site ID: 1601), Little Washita (LW; site ID: 1602), Fort Cobb (FC; site ID: 1603), Little River (LR; site ID: 1604), and Reynolds Creek (RC; site ID: 401) (blue stars in Fig. 3). Each of these networks measures SM data at a depth of 5 cm and consists of spatially intensive SM stations containing 15–30 ground-based SM observations per network.

### 3. Methodology

#### 3.1. Removing climatology SSM data

Prior to performing the TCA, we removed monthly signals by subtracting the climatology from each SSM data set. The climatology of each SSM product can be correlated and thus cause the TCA-based numbers to be over-graded. In computing the TCA and conventional error metrics, each product's anomaly was considered. The anomaly SSM (SSM<sup>a</sup>) data was calculated using the following Eq. (1):

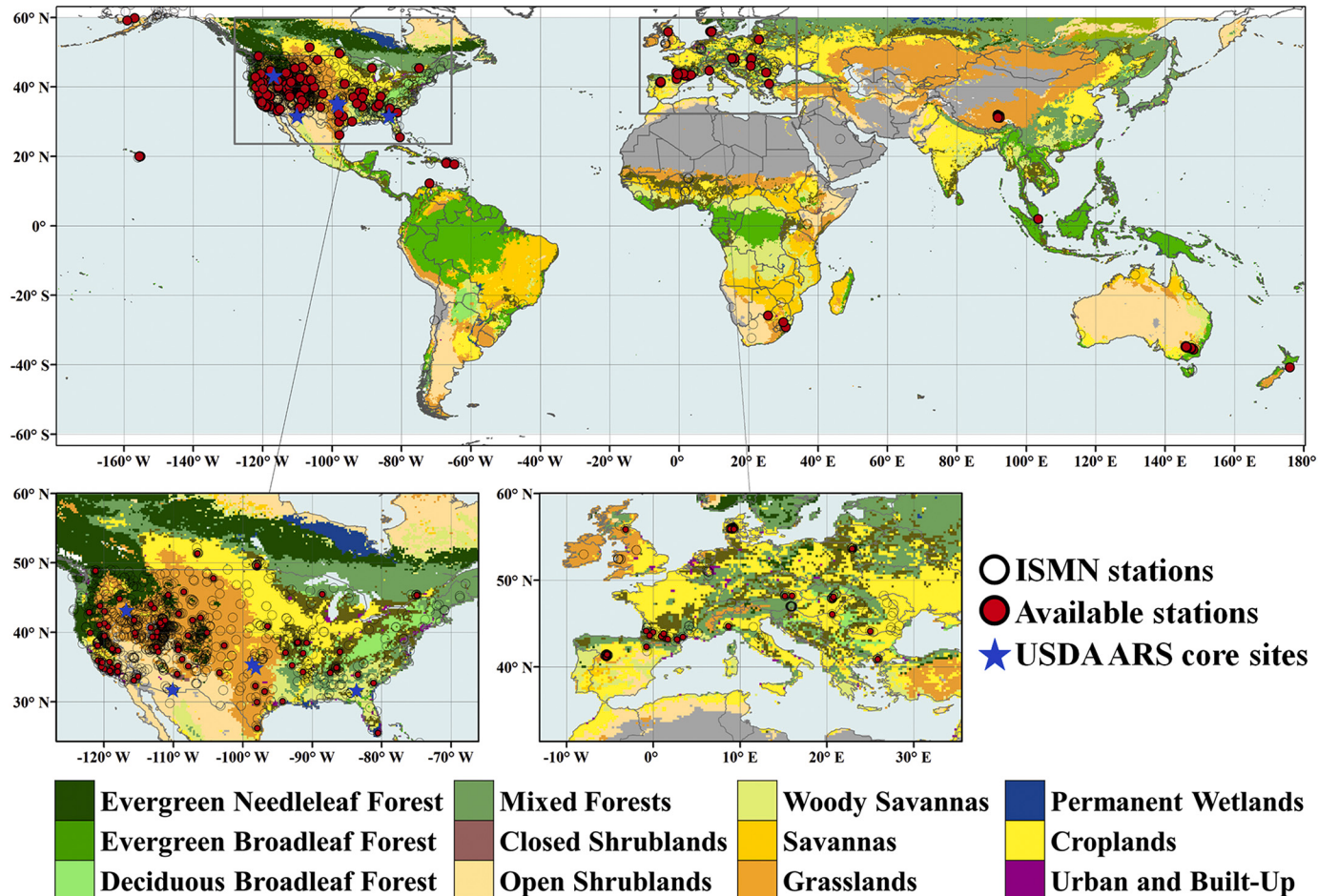


**Fig. 3.** Locations of dense (blue stars) and sparse (black circles) SM stations with IGBP-based land cover classifications as background. The ground observations are those which were commonly available for all four satellites, and only two model-based products were considered. Five ARS core sites were used, and 180 ISMN stations (red filled circles) met the conditions required for the current research. The majority of stations are concentrated in CONUS and European countries. The number of ISMN stations shown above represents the stations that passed the quality control and cross-screening processes. (For interpretation of the references to colour in this figure legend, the reader is referred to the web version of this article.)

$$SSM_{(i,j)}^a(doy, year) = SSM_{(i,j)}(doy, year) - E[SSM_{(i,j)}(month, year)] \quad (1)$$

where doy is day of year,  $i$  and  $j$  indicate the location of the target pixel.  $E[\cdot]$  calculates the expectation of each specific year's monthly averaged SSM value corresponding to its day of the year.

### 3.2. Triple collocation error estimators

In the present study, TCA was employed to evaluate satellite and model-based SSM data. The main reason for using TCA is that it does not require the assumption that the reference data sets are of high quality (Dong and Crow, 2017; Gruber et al., 2016; Stoffelen, 1998) and allows estimation of the total error variance of three independent SSM measurements. In TCA, the errors of SSM data sets are assumed to be mutually independent and orthogonal to the truth (Yilmaz and Crow, 2014). Based on this consideration, SSM products that might contain cross-correlated errors were not used in the same triplet. From the 6 SSM products, 20 triplets were considered possible ( ${}_6C_3$ ), and 10 triplets were possible for each product (Table 1). However, different triplets had the potential to violate the basic TCA assumptions for various reasons: 1) Sampling time mismatch can occur among satellites. For example, ASCAT and SMAP would have little difference in overpass time (9:30 am and 6:00 am); however, ASCAT and AMSR2 have significantly different overpass times (9:30 am and 1:30 am); thus difference in overpass time violates the TCA assumption that all data sets depict the same physical variable (flag 1). The ERA5 and GLDAS data sets were reconstructed from UTC time-based to local time-based in order to match the ASCAT, SMAP, SMOS, and AMSR2 local overpass times. These reconstructions were performed by considering the navigational time zone based on longitude and by neglecting local statutory deviations (Kim et al., 2018). 2) A sampling depth mismatch is obvious for all products. It is assumed that longer wavelength-based SSM retrievals represent deeper layers of soil; however, with different vegetation, moisture, and vegetation conditions, the representation depth can vary (please refer to Section 4.1 for further details). In addition, we used GLDAS 0–10 cm SSM, which may not represent the same soil layer as the other data sets, thereby violating the basic assumption of TCA that all data sets depict the same physical variable (flag 2). 3) If SSM were retrieved from a similar wavelength, error characteristics that are related to that wavelength could be correlated; for instance, L-band is more sensitive to RFI (flag 3). 4) If a similar retrieval algorithm for SSM was used, the final product could be highly correlated; for instance, SMAP and AMSR2 both use a radiative transfer model (Konings et al., 2011) (although the details vary to a certain degree) as a passive microwave system (flag 4). 5) Simultaneous use of both model-based products can be risky. There are differences between off-line and coupled land surface models; however, the simultaneous use of both model-based products may imperil the mutual error independence results underlying the application of TCA (flag 5). 6) If a product is combined or assimilated into another system, the two data sets should not be considered together. For example, the ASCAT SSM data were assimilated into ERA5; therefore, considering the triplet of SMAP, AMSR2, and ERA5 rather than the triplet of SMAP, ASCAT, and ERA5 triplet is important to avoid cross-correlations of ASCAT and ERA5 products (flag 6) (please refer to Section 4.1 for further details). In this study, we considered all triplets in which the sum of the flags was less than 5 (final column in Table 1) and calculated the median and standard deviation of TCA-based numbers for each product.

#### 3.2.1. Relative error variance

In order to evaluate and intercompare the error variances of four satellites and two model-based SSM data sets based on the TCA, we calculated relative error variance rather than absolute error variance. Calculation of the relative error variance is a rescaling process that uses one product as a reference and scales the other two products to the reference product. This allows accommodation of the different units

and SSM sensitivities of the various products, thus overcoming the dependency of scaled error variance patterns on the spatial climatology of the chosen reference product (Draper et al., 2013; Gruber et al., 2016).

The three independent, spatially and temporally collocated SSM data sets which are shown in Table 1 are assumed to be linearly related to the true signal ( $\theta$ ) as follows:

$$\begin{aligned} x &= a_x\theta + b_x + \varepsilon_x \\ y &= a_y\theta + b_y + \varepsilon_y \\ z &= a_z\theta + b_z + \varepsilon_z \end{aligned} \quad (2)$$

where  $a_x$ ,  $a_y$ , and  $a_z$  are systematic multiplicative biases (or scaling factors), and  $b_x$ ,  $b_y$ , and  $b_z$  are additive biases with respect to the  $\theta$ , respectively. The  $\varepsilon_x$ ,  $\varepsilon_y$ , and  $\varepsilon_z$  represent the random error of each product.

We derived the error variance from a covariance notation (Gruber et al., 2016). This approach uses the variances and covariances of data sets. The notation for the error model described in Eq. (2) is considered to be the sum of two random variables,  $\theta$  and  $\varepsilon_i$ . The variance and covariance of the SSM data sets can be described as follows:

$$\sigma_i^2 = a_i^2\sigma_\theta^2 + 2a_i\sigma_{\theta\varepsilon_i} + \sigma_{\varepsilon_i}^2 \quad (3)$$

$$\sigma_{ij} = a_i a_j \sigma_\theta^2 + a_j \sigma_{\theta\varepsilon_i} + a_i \sigma_{\theta\varepsilon_j} + \sigma_{\varepsilon_i\varepsilon_j} \quad (4)$$

where  $i, j \in [x, y, z]$  ( $i \neq j$ ).  $\sigma_i^2$ ,  $\sigma_{ij}$ , and  $\sigma_\theta^2$  are variance, covariance, and variance of the true jointly observed SSM data signal, respectively. Under the assumption of error orthogonality and zero error-cross correlation, the terms  $\sigma_{\theta\varepsilon_i}$  and  $\sigma_{\varepsilon_i\varepsilon_j}$  ( $i \neq j$ ) are equal to 0. Thus, Eqs. (3) and (4) are simplified into the following:

$$\sigma_i^2 = a_i^2\sigma_\theta^2 + \sigma_{\varepsilon_i}^2 \quad (5)$$

$$\sigma_{ij} = a_i a_j \sigma_\theta^2 \quad (6)$$

By combining the covariance of each product, the  $a_i a_j$ , which is also

**Table 1**  
Possible triplets and corresponding flags and flag sum values.

	Triplets			Flags	Flag sum
	x	y	z		
1	ASCAT	SMOS	AMSR2	1	1
2	SMOS	AMSR2	ERA5	1	1
3	ASCAT	SMOS	SMAP	2	2
4	ASCAT	SMOS	GLDAS	2	2
6	ASCAT	SMAP	GLDAS	2	2
7	ASCAT	AMSR2	GLDAS	1,2	3
8	SMOS	AMSR2	GLDAS	1,2	3
9	SMOS	SMAP	ERA5	3	3
10	AMSR2	SMAP	ERA5	1,2	3
11	ASCAT	AMSR2	SMAP	1,4	5
12	SMOS	SMAP	GLDAS	2,3	5
13	ASCAT	SMAP	ERA5	6	6
14	ASCAT	SMOS	ERA5	6	6
15	SMOS	AMSR2	SMAP	1,2,3	6
16	ASCAT	AMSR2	ERA5	1,6	7
17	SMOS	ERA5	GLDAS	2,5	7
18	AMSR2	SMAP	GLDAS	1,2,4	7
19	AMSR2	ERA5	GLDAS	2,5	7
20	SMAP	ERA5	GLDAS	2,5	7
21	ASCAT	ERA5	GLDAS	2,6	8

Flags:

- 1: sampling time mismatch.
- 2: depth mismatch.
- 3: similar frequency band for SSM retrievals.
- 4: similar SSM retrieval algorithm based on similar radiative transfer models.
- 5: simultaneous use of both model-based products.
- 6: ASCAT assimilated into ERA5.

called the sensitivity of SSM, can be estimated:

$$\begin{aligned} a_x^2 \sigma_{\theta}^2 &= \frac{\sigma_{xy} \sigma_{xz}}{\sigma_{yz}} \\ a_y^2 \sigma_{\theta}^2 &= \frac{\sigma_{yx} \sigma_{yz}}{\sigma_{xz}} \\ a_z^2 \sigma_{\theta}^2 &= \frac{\sigma_{zx} \sigma_{zy}}{\sigma_{xy}} \end{aligned} \quad (7)$$

By substituting  $a_i^2 \sigma_{\theta}^2$  in Eq. (5) with the covariance term of the three data sets shown in Eq. (7), the error variance ( $\sigma_{\epsilon_i}^2$ ) of each data set can be calculated without knowing the true value of SSM:

$$\begin{aligned} \sigma_{\epsilon_x}^2 &= \sigma_x^2 - \frac{\sigma_{xy} \sigma_{xz}}{\sigma_{yz}} \\ \sigma_{\epsilon_y}^2 &= \sigma_y^2 - \frac{\sigma_{yx} \sigma_{yz}}{\sigma_{xz}} \\ \sigma_{\epsilon_z}^2 &= \sigma_z^2 - \frac{\sigma_{zx} \sigma_{zy}}{\sigma_{xy}} \end{aligned} \quad (8)$$

To estimate the relative error variance, we calculated the fractional mean-square-error MSE (fMSE) metric (Draper et al., 2013). Draper et al. (2013) originally introduced the fractional root-mean-square-error (fRMSE), and Gruber et al. (2016) used fMSE in their study for reasons of consistency. The lower/higher the fMSE values, the more precise/noisier signal from the SSM products with the noise ranging from 0 to 1. A value of fMSE lower than 0.5 indicates that the SSM signal was stronger than its noise. The fMSE can be calculated from the variance and (Eq. (9)):

$$fMSE_i = \frac{\sigma_{\epsilon_i}^2}{\sigma_i^2} = \frac{\sigma_{\epsilon_i}^2}{a_i^2 \sigma_{\theta}^2 + \sigma_{\epsilon_i}^2} = \frac{1}{SNR + 1} \quad (9)$$

where  $i, j \in [x, y, z]$  ( $i \neq j$ ), and SNR is the signal-to-noise ratio  $\left(a_i^2 \frac{\sigma_{\theta}^2}{\sigma_{\epsilon_i}^2}\right)$ .

Investigating the individual SSM product's sensitivity with its own noise variance provides a strong advantage over absolute error estimations. To be specific, the fMSE allows investigation of an actual data set's data quality and also removes the dependency of error patterns from the reference data (Gruber et al., 2016; Su et al., 2014a).

To ensure the robustness of our results, we did not perform TCA when the correlation of any two products was lower than 0.3 and when we had fewer than 100 data samples. We calculated the median and standard deviations of the  $fMSE_i$  from each product's possible triplets when the flag sum was less than 5 (Table 1). The higher the standard deviation of the fMSE, the less robust the TCA-based results. We considered pixels in which the standard deviation of the fMSE was greater than 0.2 as having non-robust TCA-based results.

### 3.3. Conventional error estimators

In addition to TCA-based fMSE, the performance of each SSM data was investigated by conventional four metrics using in-situ SM data sets described in Section 2.5:

$$\text{Conventional} - bias = E[(\hat{\theta} - \theta)] \quad (10)$$

$$\text{Conventional} - fMSE = \frac{E[(\hat{\theta} - \theta)^2]}{E[(\hat{\theta} - E[\hat{\theta}])^2]} \quad (11)$$

$$\text{Conventional} - ubRMSE = E[((\hat{\theta} - [E(\hat{\theta})]) - (\theta - E[\theta]))^2] \quad (12)$$

$$\text{Conventional} - R = \frac{E[(\hat{\theta} - [E(\hat{\theta})])(\theta - E[\theta])]}{\sqrt{E[(\hat{\theta} - E[\hat{\theta}])^2]} \sqrt{E[(\theta - E[\theta])^2]}} \quad (13)$$

where  $E[\cdot]$  computes the expectation value,  $\hat{\theta}$  represents the SSM from satellite- or model-based SSM, and  $\theta$  is the SSM obtained from in-situ

observations.

Since we have limited ground stations that provide SM globally, we will compare TCA-based fMSE with the conventional metrics to confirm the feasibility of TCA-based fMSE for the global-scale SSM error estimators (Section 4.2). The in-situ SSM data were obtained from a few dense in-situ core sites in CONUS and sparse sites from ISMN as described in (Section 2.5).

## 4. Results and discussion

### 4.1. Detailed investigations of flags

In Section 3.2, we assigned lower flag values for violation of TCA assumptions caused by 1) sampling time mismatch, 2) depth mismatch, and 3) similar frequency bands for SSM retrievals because these particular violations are inevitable with current satellite SSM retrieval systems. Specifically, satellites in sun-synchronous orbits provide only one to two SSM observations per day at certain overpass times; and for the satellite-based SSM products used in this study, SSM retrievals were available only from the L-, C-, and X-bands. Mathematically, for 1) and 2) flags, depth mismatch and sampling time mismatch would cause a nonorthogonal error ( $\zeta$ ), which would impact the scales of the total error variances (Dong and Crow, 2017). If we assume the three zero mean anomaly SSM data,  $x$ ,  $y$ ,  $z$ , and  $x$  data with different depth (or overpass time), the error models can be described as follows:

$$\begin{aligned} x &= a_x(\theta + \zeta) + \epsilon_x \\ y &= a_y\theta + \epsilon_y \\ z &= a_z\theta + \epsilon_z \end{aligned} \quad (14)$$

Under the TCA assumptions, which state that the error of three products is mutually independent and orthogonal to the true data, the ratio of scaling factors for anomalies  $x$  and  $y$  SSM data can be calculated as follows (Dong and Crow, 2017; Draper et al., 2013):

$$a_y^* = \frac{x^T z}{y^T z} = \frac{a_x}{a_y} \quad (15)$$

$$a_z^* = \frac{x^T y}{y^T z} = \frac{a_x}{a_z} \quad (16)$$

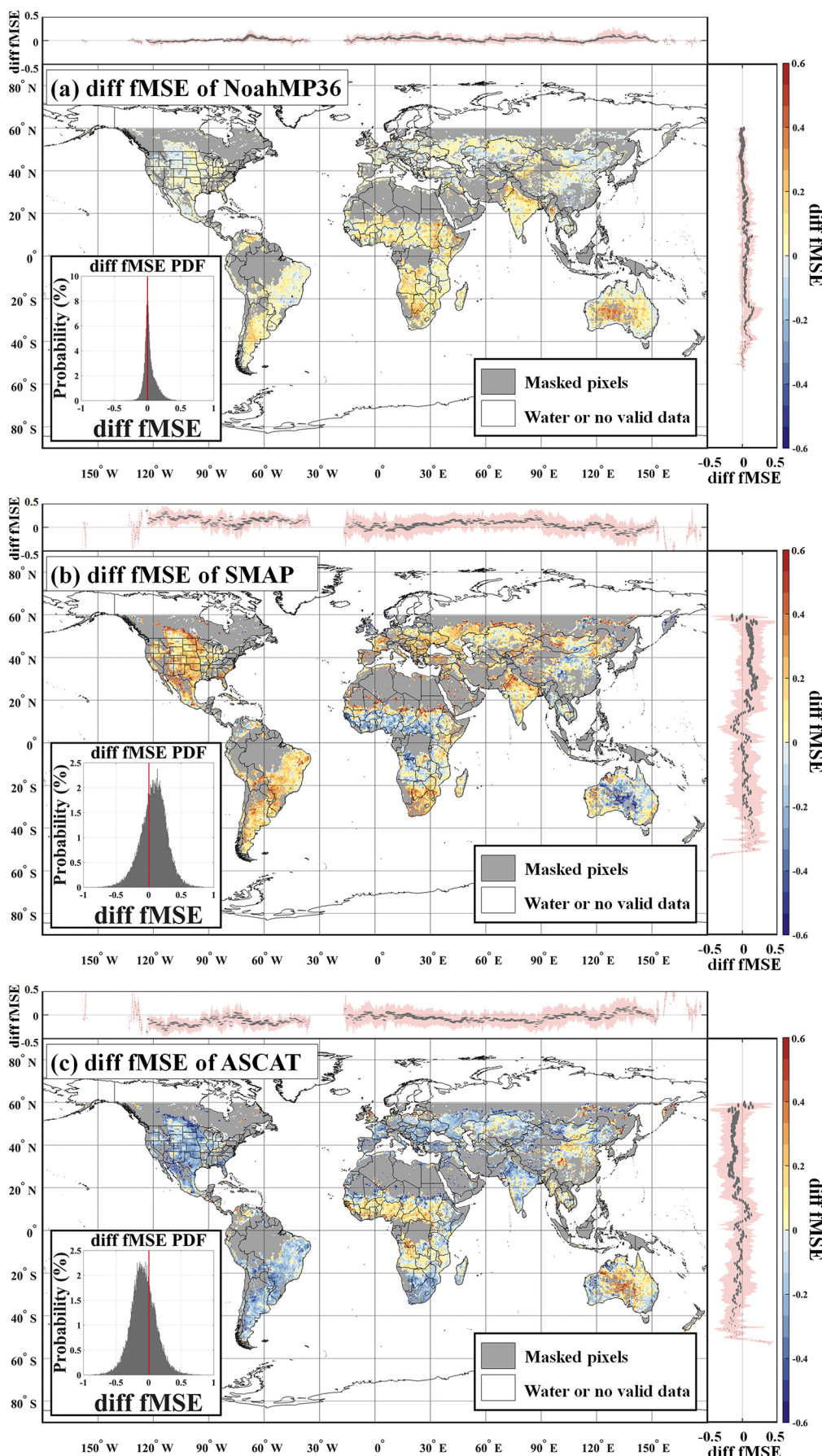
where  $\sigma_{\theta}^2$  is the variance of the true SSM. The total error covariances of anomaly  $y$  and  $z$  SSM data are estimated as follows:

$$\begin{aligned} \sigma_{\epsilon_i}^2 &= \frac{\sigma_{\theta}^4}{a_i^2} E \left[ \left( a_i^* \frac{(\sigma_{\theta}^2 + \sigma_{\zeta\theta})}{\sigma_{\theta}^2} i - x \right)^T \left( a_i^* \frac{(\sigma_{\theta}^2 + \sigma_{\zeta\theta})}{\sigma_{\theta}^2} i - a_j^* \frac{(\sigma_{\theta}^2 + \sigma_{\zeta\theta})}{\sigma_{\theta}^2} j \right) \right] \\ &= \frac{1}{a_i^2} E \left[ \left( a_i^* i - \frac{\sigma_{\theta}^2}{(\sigma_{\theta}^2 + \sigma_{\zeta\theta})} x \right)^T (a_i^* i - a_j^* j) \right] \\ &= \frac{1}{a_i^2} E \left[ \left( \frac{x^T i}{i^T j} i - \frac{\sigma_{\theta}^2}{(\sigma_{\theta}^2 + \sigma_{\zeta\theta})} x \right)^T \left( \frac{x^T i}{i^T j} i - \frac{x^T j}{i^T j} j \right) \right] \end{aligned} \quad (17)$$

where  $i, j \in [y, z]$  ( $i \neq j$ ), and  $E[\cdot]$  computes the expectation value, and  $\sigma_{\zeta\theta}$  is the covariance of the true SSM (combined with the non-orthogonal error). Under the assumption of the zero mean error, Eq. (17) is the same as  $1/a_i^{*2} \sigma_{\epsilon_i}^{*2}$ . This is equivalent to the result of Dong et al. (2017). The fMSE of  $y$  and  $z$  with the existence of nonorthogonal errors can be calculated as follows:

$$fMSE_i = \frac{\frac{1}{a_i^{*2}} \sigma_{\epsilon_i}^{*2}}{\frac{1}{a_i^{*2}} \sigma_i^2} = \frac{\sigma_{\epsilon_i}^2}{\sigma_i^2} \quad (18)$$

where  $i, j \in [y, z]$  ( $i \neq j$ ). This equation is the same as Eq. (9) above. At the same time, the  $fMSE_x$  can be biased due to additive bias caused by the nonorthogonal error. Specifically, the total error variance of



(caption on next page)

**Fig. 4.** (a) Difference between fMSE value of NoahMP3.6 calculated from the two different triplets: 1) fMSE of open-loop NoahMP3.6, SMAP, and ASCAT and 2) fMSE of SMAP assimilated NoahMP3.6 + SMAP, SMAP, and ASCAT. (b) same as (a) but for fMSE value of SMAP. (c) same as (a) but for fMSE value of ASCAT. The positive (negative) value indicates the fMSE is overvalued (undervalued) if the TCA assumption violation type falls under flag 6 (Section 3.2).

anomaly  $\mathbf{x}$  data under the assumption that the error of the three products is mutually independent and orthogonal to the truth can be calculated as follows:

$$\begin{aligned} E[(\mathbf{x} - \mathbf{a}_y^* \mathbf{y})^T (\mathbf{x} - \mathbf{a}_z^* \mathbf{z})] \\ = (a_x - a_y^*) (a_x - a_z^*) \sigma_\theta^2 + (a_x - a_y^*) a_x \sigma_{\varphi}^2 + (a_x - a_z^*) a_x \sigma_\varphi^2 + a_x^2 \sigma_\varphi^2 + \sigma_{\varepsilon_x}^2 \\ = \sigma_{\varepsilon_x}^2 c (a_x - a_y^*) (a_x - a_z^*) \sigma_\theta^2 + (2a_x^2 - a_x a_y^* - a_x a_z^*) \sigma_{\varphi}^2 + a_x^2 \sigma_\varphi^2 \quad (19) \end{aligned}$$

where  $\mathbf{x}$ ,  $\mathbf{y}$  and  $\mathbf{z}$  are the anomaly SSM data sets. The fMSE of  $\mathbf{x}$  data with the existence of the nonorthogonal errors can be calculated as follows:

$$fMSE_x = \frac{E \left[ \left( \mathbf{x} - \frac{\mathbf{x}^T \mathbf{z}}{\mathbf{y}^T \mathbf{z}} \mathbf{y} \right)^T \left( \mathbf{x} - \frac{\mathbf{x}^T \mathbf{z}}{\mathbf{y}^T \mathbf{z}} \mathbf{z} \right) \right] - ((a_x - a_y^*) (a_x - a_z^*) \sigma_\theta^2 + (2a_x^2 - a_x a_y^* - a_x a_z^*) \sigma_{\varphi}^2 + a_x^2 \sigma_\varphi^2)}{\sigma_x^2} \quad (20)$$

This equation shows that with the existence of the nonorthogonal errors,  $fMSE_x$  will be biased. Thus, the error caused by the nonorthogonal errors such as depth mismatch would affect the  $fMSE_x$ .

Analytic calculations and quantifications of possible bias caused by the violation of TCA assumptions are challenging tasks. Specifically, violations of flags 4, 5, and 6 can certainly cause errors beyond the nonorthogonal error. However, the violations classified in flags 4, 5, and 6 are distinguishable violations that the researcher can clearly avoid; thus, these flags should not be deliberately ignored. Therefore, we assigned higher flag values to penalize triplets, which are regarded as intentional violations of TCA assumptions. Composing triplets with two model-based SSM values ( $\mathbf{x}$  and  $\mathbf{y}$ ) (e.g., Noah-Multiparameterization (NoahMP)3.6 and NoahMP4.0 (flag 5)) of the same forcing variables (e.g., MERRA-2 forcing) and satellite-based SSM ( $\mathbf{z}$ ) would greatly degrade the performance of  $\mathbf{z}$  data. The relative total error variance of  $\mathbf{x}$  and  $\mathbf{y}$  data is very likely to be biased. Similarly, TCA metrics from a triplet of SSM data taken from LSMs ( $\mathbf{x}$ ) without data assimilation (DA) of satellite SSM data ( $\mathbf{y}$ ) (i.e., open-loop LSM's SSM), satellite-based SSM which is assimilated in  $\mathbf{x}$ , and third SSM data ( $\mathbf{z}$ ) (flag 6), would be biased.

In order to demonstrate the possible fMSE bias that can be caused by violations of the TCA assumptions marked as flags 6, we assimilated SMAP SSM data into NoahMP3.6 using LIS (Kumar et al., 2006) and conducted TCA. Fig. 4 shows the difference between the fMSE values for NoahMP3.6, SMAP, and ASCAT calculated from two different triplets: 1) open-loop NoahMP3.6, SMAP, and ASCAT SSM data, and 2) SMAP assimilated NoahMP3.6, SMAP, and ASCAT SSM data sets. The positive (negative) value indicates the data performance is overvalued (undervalued) due to the combination of SMAP assimilated NoahMP3.6 and SMAP data in composing a triplet. Fig. 4 clearly demonstrates that if we violate the TCA assumption indicated as flag 6 (Section 3.2), the fMSE values of NoahMP3.6 ( $\mathbf{x}$ ) and SMAP ( $\mathbf{y}$ ) are likely to be overvalued and ASCAT ( $\mathbf{z}$ ) is likely to be undervalued as SMAP data is assimilated into NoahMP3.6. In addition, just as we avoided composing triplets with ASCAT and ERA5 data, we did not consider ESA-CCI SSM merged products in this study (Dorigo et al., 2017). Since ESA-CCI merges ASCAT, SMOS, and AMSR2 SSM data, triplets composed of ESA-CCI and the two satellite-based SSM data sets used in this study would cause bias in TCA-based numbers. In other words, it would violate the TCA assumption that the errors of the three products are mutually independent (Draper et al., 2013).

#### 4.2. Evaluation of SSM satellite- and model-based products using in-situ SM networks and viability of TCA-based median fMSE for global-scale error analysis

In this section, we compared the TCA-based fMSE with four conventional error estimators (i.e., bias, fMSE, correlation coefficient R, and ubRMSE) which were calculated for each SSM product (i.e., ASCAT, SMOS, ASMR2, SMAP, ERA5, and GLDAS). The goal of employing spatially intensive SM observations core sites is to investigate the feasibility and reality of TCA-based fMSE in comparison to conventional relative evaluation metrics and absolute evaluation metrics. Dense

watershed networks can be used to calculate absolute error metrics as they are composed of 15–60 ground observations per watershed site. Thus, the representative error caused by the spatial resolution mismatch between point-scale observations and gridcell-scale SSM retrievals can be minimized by weighting the SM stations based on the Voronoi diagram technique and arithmetic average (Colliander et al., 2017; Crow et al., 2012). Many previous studies have used such dense ground SM observation data and up-scaling approaches to evaluate remotely-sensed and model SSM data sets (Chen et al., 2017; Colliander et al., 2017; Dong et al., 2020). However, the limited number of dense networks hampers the evaluation of gridcell-scale SSM data from diverse environmental conditions. Thus, researchers use data from sparse SM networks to evaluate the error characteristics of satellite and model SSM data sets until more networks with different conditions are available. These networks are often called “sparse” because they are usually not spatially distributed with small number of ground observations for a gridcell-scale, although the large number of sites in a network compensate for the sparse distribution of ground observations (Al-Yaari et al., 2019b; Brocca et al., 2011; Dorigo et al., 2011, 2013; Kim et al., 2018). Despite the degradation of absolute evaluation metrics caused by representative errors in sparse networks, Dong et al. (2020) analytically demonstrated that representative errors do not impact the relative accuracy assessment of SSM derived from different gridcell-scale SSM data sources. For these reasons, for the sparse network location, we compared TCA-based fMSE with R-values calculated from ISMN SM data sets.

Fig. 5 shows the comparison results between the TCA-based fMSE (red boxes with left y-axis) and conventional fMSE (blue boxes with right y-axis) calculated from the SM data obtained with dense ground observations. In Fig. 5(a), it is clear that the TCA-based fMSE results are very similar to the ground-based fMSE calculations. It is worth noting that in-situ-based fMSE is theoretically higher than TCA-based values as in-situ SSM MSE is lower than satellite- or model-based MSE, which leads to a positive bias in conventional fMSE. Likewise, the TCA-based fMSE shows lower values (less noisy data) for higher R-value (less noisy data) data sources. These results are very encouraging as they show the strong feasibility of TCA-based metrics for assessment of relative error characteristics from different SM data sources. Fig. S1 is the same as Fig. 5(b), except that, the conditional R-values were calculated based on the 180 ground stations from ISMN (bias and ubRMSE results are discussed in Section 4.4.). It is interesting to note very similar results are obtained in terms of TCA-based fMSE considering dense (Fig. 5(b)) or sparse (Fig. S1) SSM networks.

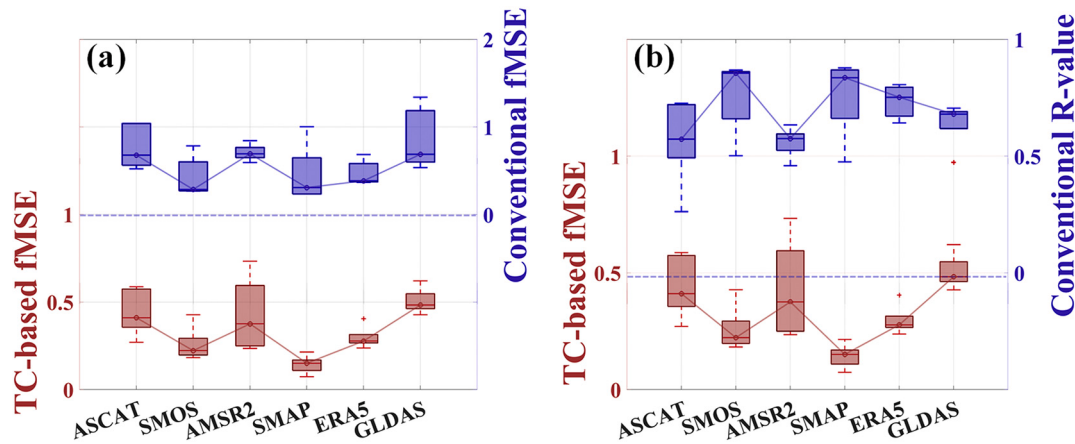


**Fig. 5.** (a) Boxplots of the TCA-based fMSE (Eq. (9)) (red; left y-axis) and the conventional fMSE (Eq. (11)) (blue; right y-axis) for ASCAT, SMOS, AMSR2, SMAP, ERA5, and GLDAS. (b) Boxplots of the TCA-based fMSE (Eq. (9)) (red; left y-axis) and the conventional correlation coefficient (R) value (Eq. (13)) (blue; right y-axis) for ASCAT, SMOS, AMSR2, SMAP, ERA5, and GLDAS. Conventional metrics were calculated using dense SM ground observations. (For interpretation of the references to colour in this figure legend, the reader is referred to the web version of this article.)

This figure is once again consistent with the assertion that TCA-based fMSE is a robust method for error characterization and the intercomparison of SSM data sets from different sources over various gridcell-scale locations.

The importance of TCA-based error evaluation becomes even more apparent when we investigate the gridcell-scale irrigation percentage and VOD ranges of SM networks in dense and sparse locations (please refer to Table S1 for detailed information about each station used in this study). Fig. S2 shows a histogram of ground station locations with respect to different gridcell-scale irrigation percentages and VOD values. It is clear that most of these SM stations are located within pixels composed of ~9% irrigated land. However, even though there are in-situ stations located within irrigated gridcells, these stations are not usually located in irrigated farmlands; thus, they cannot capture the SM variability caused by actual irrigation activities. It follows, then, that long-term observations of SM over irrigated areas using ground stations are impossible because installing ground stations in irrigated farmland is very difficult over the long term. In contrast, in-situ stations are a viable option across a wide range of VOD values. However, these stations are most often located outside forests or in an open sapce within a tree stand and thus they do not capture the SM variability caused by the micrometeorology of the forest canopy. It is true that we have five cosmic-ray neutron probe (CRNP) stations which can overcome the limitations of ground measurement SM made using Time Domain Reflectometry, Frequency Domain Reflectometry, Transmission Line Oscillation, etc. methods (Kim et al., 2020; Nguyen et al., 2017); however, CRNP is relatively expensive, and the small number of CRNP stations also limit the use of this method in monitoring global-scale SM variability. Thus, we conclude that global-scale monitoring of SSM requires both satellite- and model-based SSM estimation, and that TCA is a critical method of evaluating these data sets.

All the results shown in this section confirm the feasibility and robustness of the TCA-based error metric for global-scale error evaluations of satellite- and model-based SSM data because it shows significantly similar performance to conventional error estimators.

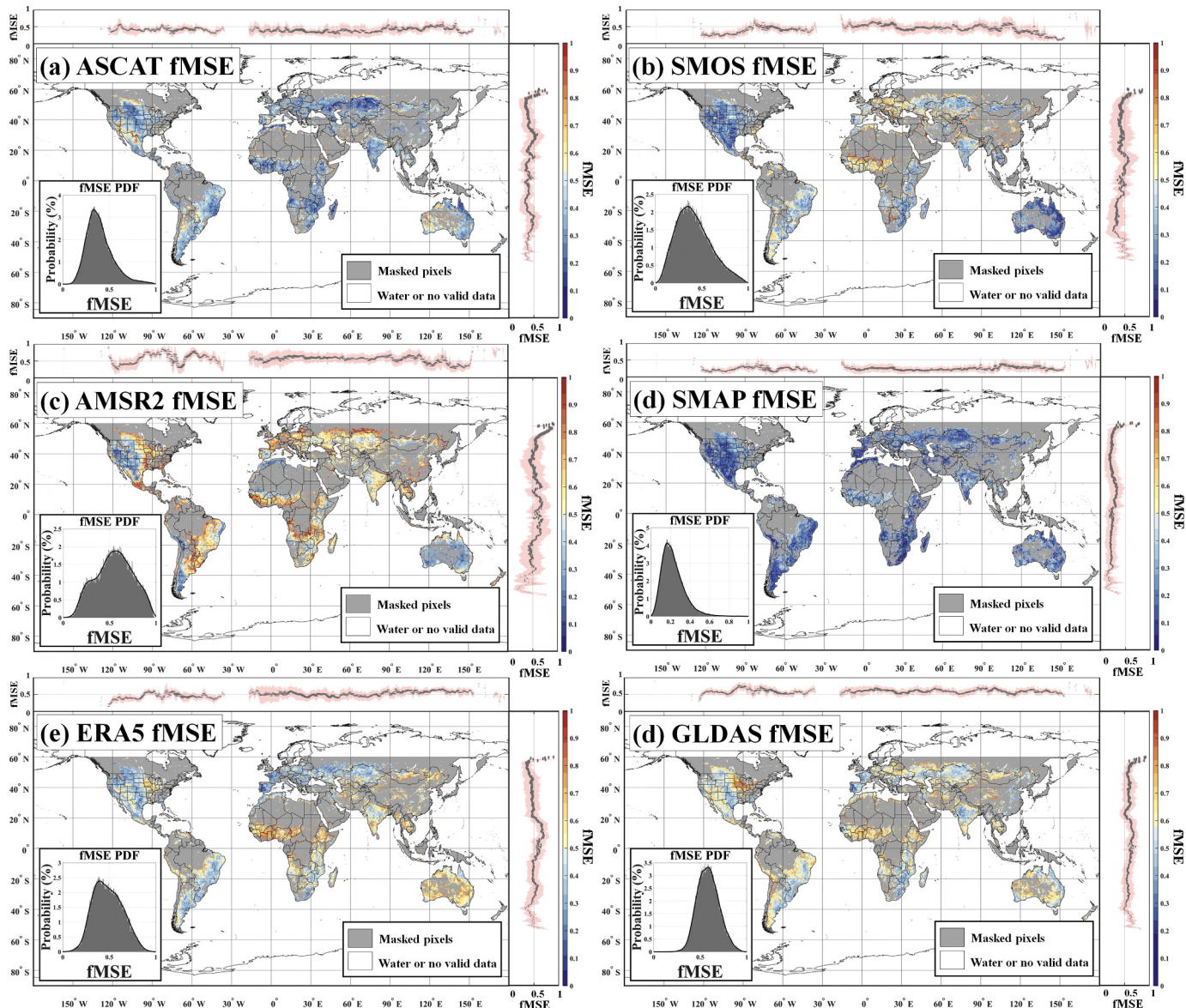
#### 4.3. Global-scale spatial patterns and inter-comparison of soil moisture data using TCA

Fig. 2 shows the global distribution of average SSM retrieved from (a) ASCAT, (b) SMOS, (c) AMSR2, (d) SMAP, (e) ERA5, and (f) GLDAS data sets from 2015 to 2019. The inset probability density function (PDF) and longitude and latitude zonal averaged SSM graphs clearly show that each satellite retrieval or model-based data has its own

distinctive spatial patterns of SSM. However, SMOS and SMAP showed very similar spatial patterns. Satellite-based SSM products and GLDAS show right-skewed (positively skewed) distribution, while ERA5 SSM exhibits a multimodal distribution.

Theoretically, the lower frequency bands of SMAP and SMOS should be better at penetrating vegetation than ASCAT and AMSR2, while SSM retrieval from dense forest areas is possible but limited (Burgin et al., 2017). A recent study also found that SMOS-IC showed meaningful SSM values over the Amazon basin (Li et al., 2020). By contrast, the model-based data sets can reproduce SSM data sets over highly vegetated areas. Overall, as expected, the satellite and model-based mean SSM values of the different climates demonstrate patterns similar to those of arid climates; i.e., they have relatively low SSM values (e.g., the Sahara Desert); or of tropical climates, meaning relatively high SSM values (e.g., the Andean Mountains). AMSR2 showed relatively high SSM latitude over 40 degrees, and it showed low SSM over tropical areas where VOD was higher than 0.6. These results indicate that low-quality AMSR2 SSM data has not been properly filtered by current data quality flags.

Based on the PDF results in each figure in Fig. 6, SMAP showed the best performance among all products. SMOS showed the best performance over Australia and similar performance to SMAP over the contiguous United States, while ASCAT showed similar performance to SMAP over European countries. AMSR2 showed the worst results over South America and Africa, but SMOS-IC also showed unanticipatedly high fMSE results. Considering that the regional patterns of the accuracy of SMOS-IC depend on RFI, unexpected relatively high fMSE spatial patterns were found in the SMOS-IC data over Africa and to a lesser extent over South America as RFI sources are relatively limited over these areas (SMOS RFI sources are mainly found in southern Europe, northern and eastern regions of Africa, India, central and southern regions of China). SMOS-IC is completely independent of ancillary data, while other products are strongly dependent on vegetation conditions, which can cause a strong autocorrelation among products due to ancillary data related to optical vegetation indices. However, we assumed that this impact was mitigated after considering all possible triplets and calculating the median of fMSE (more discussion is included in Section 4.4). Further investigations regarding the impact of vegetation on TCA will be conducted in future studies since it is out of scope for the current manuscript. Further discussions with respect to different levels of vegetation and irrigation activities and dependencies of TCA with respect to different triplets are included in the next section (Sections 4.4–4.6).



**Fig. 6.** Maps of median fMSE of (a) ASCAT, (b) SMOS, (c) AMSR2, (d) SMAP, (e) ERA5, and (f) GLDAS. Upper and right panels indicate longitude and latitude zonal means of median fMSE, respectively. Inset graphs represent PDF for each data set, marker sizes in zonal plots illustrate proportional to zonal land area, and the shaded region shows  $\pm 1$  standard deviation.

#### 4.4. Error characteristics of soil moisture data over forest regions

The plots in Fig. 7 show the histograms and cumulative distribution of median fMSE with respect to different vegetation conditions (blue bars and lines: sparsely vegetated regions, red bars and lines: moderately vegetated regions, and yellow bars and lines: densely vegetated regions) for four satellites and two modeled data sets corresponding to data obtained in Fig. 6. The  $F_{\text{fMSE}}(0.5)$  value of each plot indicates the probability of SSM data having an SSM signal stronger than its noise. Table 2 shows the results of  $F_{\text{fMSE}}(0.5)$  for different products in terms of different vegetation conditions.

We found that over densely forested areas, ASCAT, SMOS, and SMAP data showed relatively higher  $F_{\text{fMSE}}$  values than model-based SSM products (Table 2):  $F_{\text{fMSE}}(0.5|\text{Dense})$  was 0.8038, 0.6657, and 0.9840, respectively. ASCAT showed similar accuracy over densely vegetated areas as over sparsely and moderately forested areas. One plausible explanation for the good accuracy of ASCAT SSM retrievals might be increased backscatter due to vegetation matter. When Frison and Mougin (1996) investigated signatures from the European Remote

Sensing (ERS) backscatter coefficients with respect to the vegetation dynamics obtained from optical vegetation indices, they found that backscatter coefficients were highly sensitive to seasonal vegetation dynamics. This was mainly due to the natural high correlation between vegetation dynamics and increases in SSM (Al-Yaari et al., 2014b). ASCAT SSM may also gain benefits from intercepted water on the vegetation canopy, which could increase backscatter and contribute to the creation of an artificial SSM signal. Thus, increased backscatter could simultaneously aid in capturing SSM variations over densely forested areas. These vegetation-related phenomena make it very difficult to decouple the contributions of variation in SSM and plant phenology from variations in the backscatter coefficient (Wigneron et al., 1999a, 1999b). However, although variation in vegetation dynamics and SSM is not always in harmony in many climate regions, the overall performance of ASCAT SSM as indicated by TCA-based fMSE showed good results. These results indicate that we can expect an active system (i.e., ASCAT) to perform well in monitoring SSM over forest areas, and our result aligns well with Al-Yaari et al. (2014b). However, dedicated research efforts and experiments in future studies would be necessary to

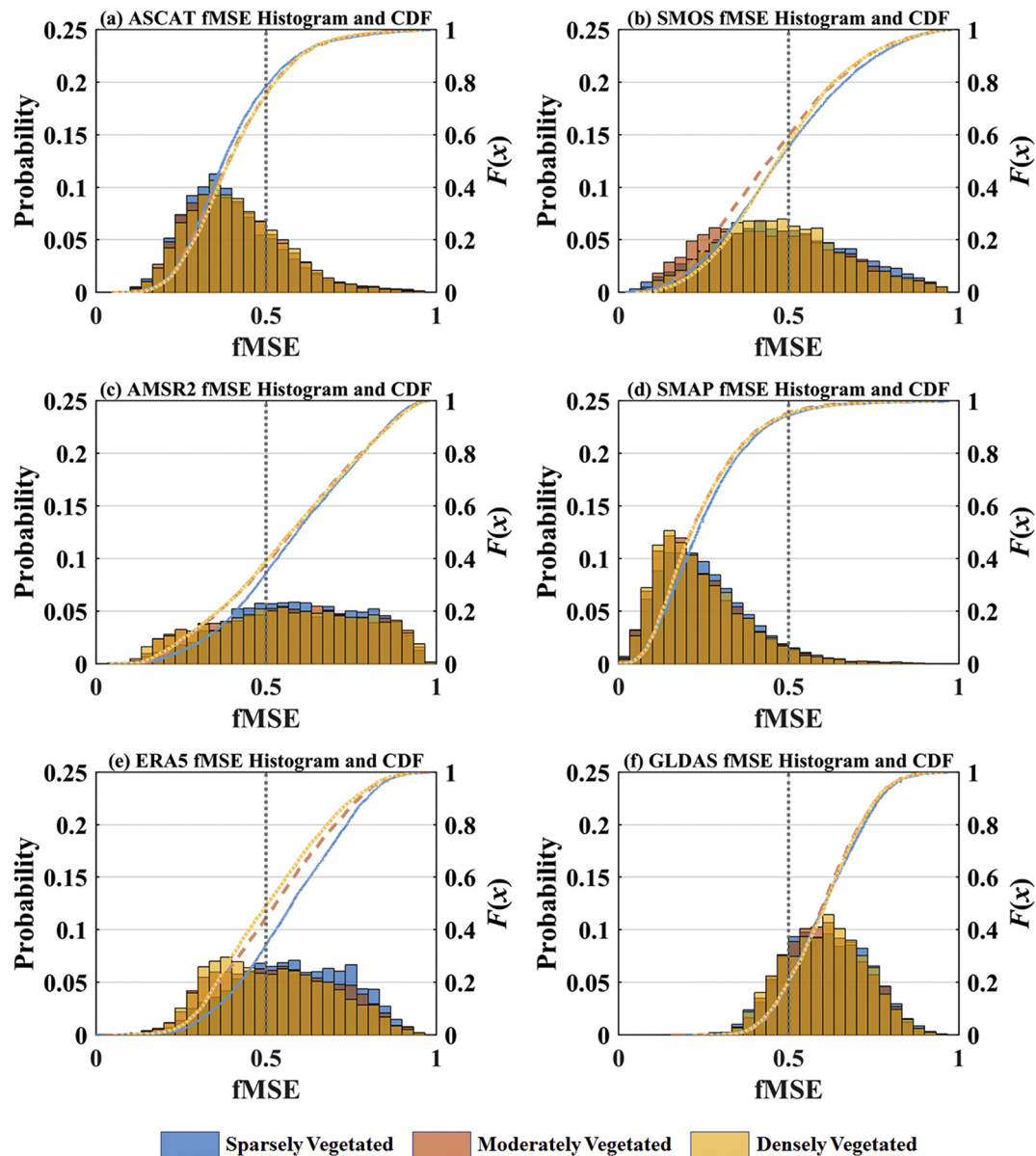


**Fig. 7.** Probability histogram and CDF of fMSE values for (a) ASCAT, (b) SMOS, (c) AMSR2, (d) SMAP, (e) ERA5, and (f) GLDAS over sparsely vegetated regions (blue bars and lines), moderately vegetated regions (red bars and lines), and densely vegetated regions (yellow bars and lines) calculated from the TCA. (For interpretation of the references to colour in this figure legend, the reader is referred to the web version of this article.)

**Table 2**

$F_{\text{fMSE}}(0.5)$  values over sparse, moderate, and dense vegetation conditions.

Vegetation	ASCAT	SMOS	AMSR2	SMAP	ERA5	GLDAS
$F_{\text{fMSE}}(0.5 \text{Sparse})$	0.7839	0.5523	0.3439	0.9450	0.3441	0.1965
$F_{\text{fMSE}}(0.5 \text{Moderate})$	0.7562	0.5981	0.3787	0.9534	0.4465	0.1971
$F_{\text{fMSE}}(0.5 \text{Dense})$	0.7527	0.5700	0.3891	0.9508	0.4917	0.2056

provide solid evidence to support the above hypothesis.

In addition, over densely vegetated regions, L-band based (i.e., SMAP and SMOS) SSM estimations are expected to perform better than the X-band frequencies of passive sensors (i.e., AMSR2). This is because higher microwave bands are easily attenuated by vegetation, making X-band-based AMSR2 LPRM SSM measurements relatively insensitive to SSM variability. In other words, AMSR2 SSM estimations over forest regions are expected to have a noise variance ( $\sigma_e^2$ ) higher than the estimated SSM variance ( $\sigma^2$ ) indicated by the  $F_{\text{fMSE}}(0.5|\text{Dense})$  value, which is lower than 0.5 (Eq. (9)) in Table 2. However, SMOS showed a

lower value  $F_{\text{fMSE}}(0.5|\text{Dense})$  than SMAP.

Several interesting features were also found in the model results: the model-based ERA5 and GLDAS data showed lower  $F_{\text{fMSE}}(0.5|\text{Dense})$  values than those of the ASCAT, SMOS, and SMAP products, having  $F_{\text{fMSE}}(0.5|\text{Dense})$  of 0.4917 and 0.2056, respectively. This result is encouraging because it indicates that satellite-based SSM in forested areas that have passed quality control processes can provide added value in model-based products and thus improve the prediction skills of model data through data assimilation (DA) having high SNR. In areas with highly vegetated conditions where active and passive microwave-based soil moisture data are masked out due to low data quality (Fig. 2), model-based SSM could provide SSM. However, if the model data show high errors, researchers may have to consider other options. For example, researchers need to decide whether they will use model-based data with low-quality SSM data and risk some uncertainty, or whether they need to consider other sources of SSM data such as the Atmospheric Land Exchange Inverse (ALEXI) model-based or Gravity Recovery and Climate Experiment-retrieved (GRACE), observationally-driven

SSM data (Anderson et al., 2007; Sadeghi et al., 2020).

Furthermore, over sparsely and moderately vegetated areas, ASCAT, SMOS, and SMAP outperform other products (Table 2). For all vegetation conditions, AMSR2 showed lower  $F_{\text{fMSE}}(0.5)$  values than ERA5. The AMSR2 C-band frequencies-based SSM product could provide better quality SSM data than the X-band, especially over vegetated areas, since the C-band can penetrate more deeply than the X-band. In the present study, for a robust TCA, we selected the X-band (Section 3.2) AMSR2 product; however, considering C-band AMSR2 SSM data for different triplets could provide different results. For sparsely vegetated areas ( $F_{\text{fMSE}}(0.5|\text{Sparse})$ ), SMOS and AMSR2 SSM products showed slightly degraded performance compared to moderately vegetated conditions ( $F_{\text{fMSE}}(0.5|\text{Moderate})$ ). Furthermore, ASCAT has a well-known issue when used in its capacity as an active sensor: it appears to be very sensitive to sub-surface heterogeneities and surface roughness due to unpredictable volume scattering from deeper soil layers over dry surfaces, resulting in a wet bias in ASCAT-based SSM estimates (Morrison and Wagner, 2019). However, in our study ASCAT

did not show significant degradation of performance over sparsely vegetated areas because these areas did not include a high fraction of sand due to our masking out of desert and barren areas based on IGBP data.

GLDAS data showed the lowest  $F_{\text{fMSE}}$  of all products. Two plausible reasons for its low TCA-based numbers is depth mismatch (0–10 cm) with satellite products (Section 4.1). Currently, the GLDAS Noah model provides SSM estimates at 0–10 cm soil layer (the topsoil layer), so a more proper comparison of GLDAS SSM TCA results can be performed with shallow-layer SSM simulations in a future study. Beck et al. (2020) also reported that, of the six model-based SSM data products, GLDAS produced the poorest results due to the quality of its precipitation forcing data. Fig. S1 shows a comparison of TCA-based fMSE and the conventional-R value calculated using SM data from the ISMN SM data, and Figs. S3 shows a comparison of TCA-based fMSE and the absolute error metrics (i.e., bias and ubRMSE) calculated using SM data from the USDA ARS core sites. The results show that the performance of GLDAS based on the results of relative and absolute errors are better than the TCA-based fMSE. This result might be due to the installation depths of

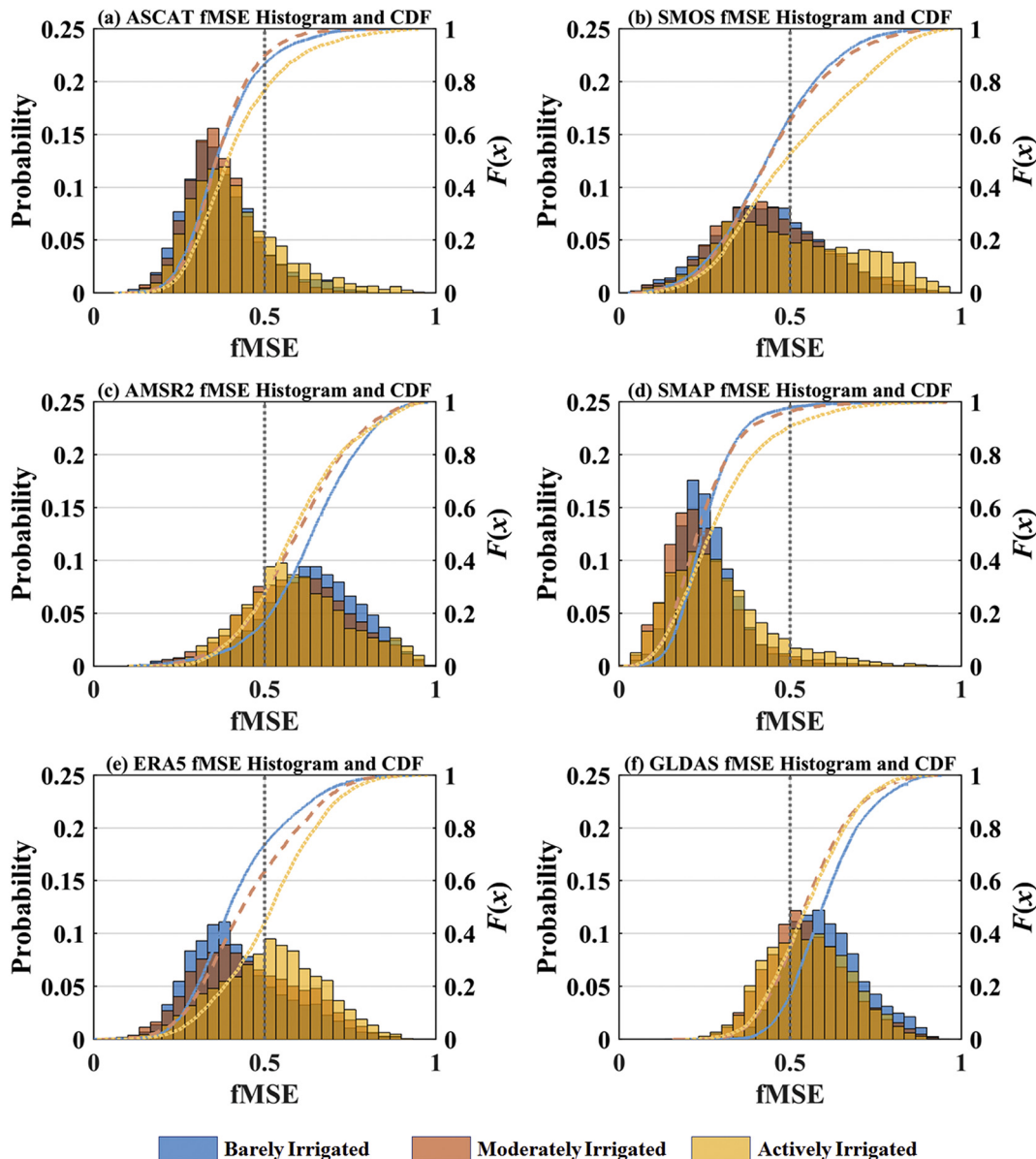


**Fig. 8.** Probability histogram and CDF of fMSE values for (a) ASCAT, (b) SMOS, (c) AMSR2, (d) SMAP, (e) ERA5, and (f) GLDAS over barely irrigated areas (blue bars and lines), moderately irrigated areas (red bars and lines), and actively irrigated areas (yellow bars and lines) calculated from the TCA. (For interpretation of the references to colour in this figure legend, the reader is referred to the web version of this article.)

SM sensors: we used ground-based SM data collected at near surface to 10 cm soil depths.

It is also important to note that none of the areas considered sparse, moderate, or densely forested included any croplands or irrigated regions (please refer to [Sections 2.1 and 2.2](#)); all the results currently obtained are assumed to be independent of irrigation activities.

#### 4.5. Error characteristics of soil moisture data over irrigated regions

The plots in [Fig. 8](#) show the same results as in [Fig. 7](#), but for different irrigation conditions (blue bars and lines: barely irrigated areas, red bars and lines: moderately irrigated areas, yellow bars and lines: actively irrigated areas) for four satellites and two model-based data sets corresponding to data obtained in [Fig. 8](#). [Table 3](#) shows the results of  $F_{\text{fMSE}}(0.5)$  for different products in terms of different irrigation conditions.

For all irrigated conditions, SMAP showed the highest  $F_{\text{fMSE}}(0.5)$  of the various products we tested; and ASCAT, SMOS, and SMAP showed better performance over actively irrigated areas than data from the two models. However, AMSR2 showed lower  $F_{\text{fMSE}}(0.5)$  than ERA5 over all irrigation conditions ([Table 3](#)). One more interesting result is that the results from ERA5 were comparable to SMOS over barely and moderately irrigated conditions. [Tuinenburg and de Vries \(2017\)](#) also found that reanalysis data can indirectly include irrigation schemes by assimilating 2-m temperature observation data; this is due to irrigation activities significantly impacting the atmosphere, and the reanalysis system consequently responding to SM variability. In addition, it is worth noting that ASCAT data was assimilated into ERA5; thus, ERA5 could include irrigation schemes. This result emphasizes the difficulty in determining whether satellite-based data is always a better alternative than model-based data over these regions, since SMOS and AMSR2 may produce more errors than ERA5. It is worth noting that ASCAT, SMOS, SMAP, and ERA5 show degraded performance as irrigation activities increase. The results of higher errors in SMOS-IC SSM data over irrigated areas may also be related to RFI. The areas of irrigation correspond well with RFI regions, especially for SMOS (high SMOS RFI and irrigation levels can be found simultaneously in India and China). This result emphasizes the careful use of SSM data which were retrieved from lower frequency systems for agricultural applications. Considering the results showing that ASCAT, SMOS, SMAP produce fewer errors than models over most irrigation conditions, satellite data have a strong potential to provide meaningful signals for DA when they are assimilated into LSMs.

Overall, these results emphasize the importance of considering several satellite and model data sources when SSM products are intercompared. In extreme cases, wrong conclusions may be reached if data from only two satellites (e.g., SMOS and AMSR2) are compared with data from one model (e.g., ERA5). For instance, these triplets for TCA over barely irrigated areas could lead to the incorrect conclusion that model-based SSM data are better than satellite-based data over irrigated areas. A similar erroneous conclusion could be reached if only ASCAT and SMAP data are compared with model products. For instance, satellite-based SSM may be assumed to perform better than model-based SSM; but this finding is erroneous, as we can see when we compare the results of AMSR2 and ERA5 (or GLDAS).

#### 4.6. Dependency of the different triplets on the TCA

In this study, we first introduced the use of several TCA triplets for one product in order to overcome the limitation of choosing the triplets to calculate robust TCA-based numbers, mitigating the violations of the basic TCA assumptions. [Fig. 9](#) shows maps of the standard deviations of fMSE (hereafter std.(fMSE)) values for the SSM data from each satellite (calculated from the triplets in which the flag sum was less than 5). These maps illustrate how the fMSE value for each pixel is spread out; in other words, it demonstrates the effect of testing other triplets to

determine the variation of each product's fMSE value. One interesting result is that the ERA5 data produced the lowest std.(fMSE). A low std.(fMSE) indicates a robust TCA result. This indicates that ERA5 has relatively low cross-correlation with other SSM data (except ASCAT) and thus can be used as a strong candidate when calculating TCA-based numbers. The GLDAS also showed lower std.(fMSE) than satellite data sets. In contrast to model-based products, clear contrasts of std.(fMSE) were found with the satellite SSM data sets. Specifically, the areas represented by red boxes showed relatively high std.(fMSE) (std(fMSE) > 0.2). If satellite-based SSM data over these areas is assessed with only a few triplets or a single triplet, biased conclusions become very likely. However, it is difficult to intercompare the std.(fMSE) of all products over the same areas, mostly because obtaining enough quality data for TCA is not possible.

#### 4.7. Advantage of selective use of satellite and model data

We conducted here an analysis to evaluate potential results from a synergistic use of satellite and model-based SSM products. In the previous sections, it was shown that over densely vegetated areas, satellite-based SSM data could perform better than model-based SSM data. By contrast, model-based SSM can perform better than certain satellite-based SSM products over barely or moderately irrigated areas. [Fig. 10\(a\)](#) shows a map of fMSE from a combination of four satellites and two model-based SSM products; we selected the lowest fMSE data from all products. It is clear that if we use SSM data selectively, we can dramatically reduce the uncertainties of SSM data on a global scale. It is also worth noting that by selecting from all available satellite and modeled data sets, we can obtain SSM data that has a stronger signal than its noise over forest or irrigated areas. [Figs. 10\(b\) and 10\(c\)](#) show that for every vegetation and irrigation condition, all  $F_{\text{fMSE}}(0.5)$  values are close to 1. Furthermore, PDFs of fMSE for every condition show very similar distributions to one other. However, as shown in [Fig. 10\(a\)](#), many areas still cannot be investigated because it is impossible to select appropriate triplet components for TCA. For example, over the Amazon regions, the triplet should consist of two satellite and modeled or three satellite data sets. However, as shown in [Section 4.4](#), it was impossible to obtain microwave satellite-based SSM data over very densely vegetated areas because low-quality data are anticipated and thus masked out based on quality flags. Similarly, we were unable to make appropriate triplets over desert areas such as the Middle East and East Asia. To overcome the limitation of acquiring three independent variables for TCA, several studies have proposed methods that use only two variables ([Dong et al., 2019b; Su et al., 2014b](#)). However, these approaches may not be appropriate for the current analysis since the SSM variable could have strong error auto-correlations and thus lead to significantly biased results.

In this results section, we have shown four main findings:

- 1) We showed that the results from TCA-based and conventional metrics are consistent. These results imply that TCA can be utilized to estimate relative errors over areas where ground-based SSM data are not available.
- 2) We found that considering TCA statistics from a single triplet can be biased. This indicates that TCA from various triplets for specific data sets can result in more robust TCA statistics.
- 3) We demonstrated that the performance of satellite-based SSM data

**Table 3**  
 $F_{\text{fMSE}}(0.5)$  values over bare, moderate, and active irrigation conditions.

Irrigation	ASCAT	SMOS	AMSR2	SMAP	ERA5	GLDAS
$F_{\text{fMSE}}(0.5 \text{Bare})$	0.8681	0.6688	0.1709	0.9784	0.7364	0.1698
$F_{\text{fMSE}}(0.5 \text{Moderate})$	0.8973	0.6533	0.2764	0.9664	0.6344	0.3433
$F_{\text{fMSE}}(0.5 \text{Active})$	0.7671	0.5266	0.2734	0.9075	0.4402	0.3512

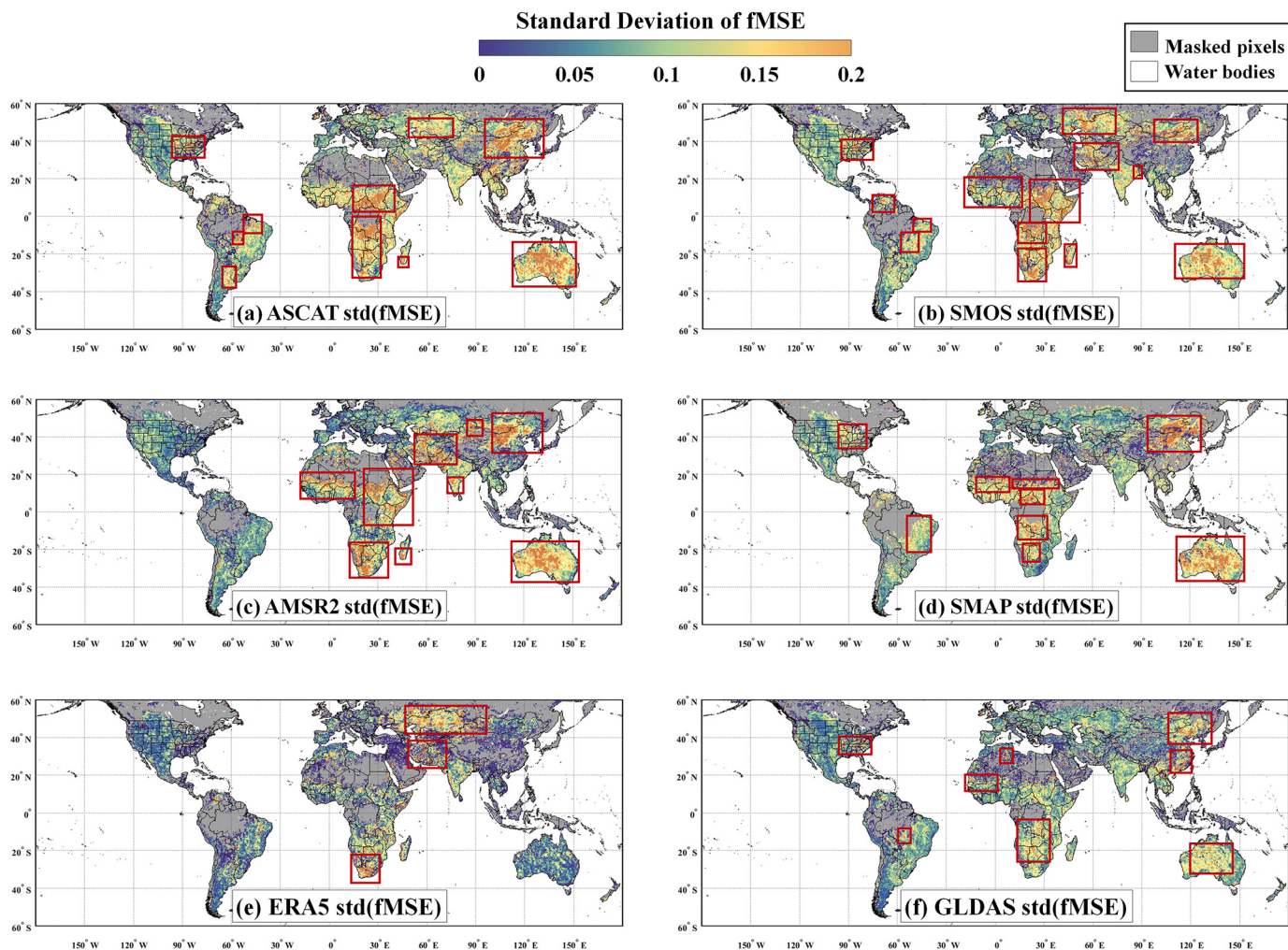


**Fig. 9.** Maps of the standard deviation of fMSE for (a) ASCAT, (b) SMOS, (c) AMSR2, (d) SMAP, (e) ERA5, and (f) GLDAS.

should not always be regarded as less accurate than model-based SSM over vegetated areas; and similarly, model-based data should not always be regarded as more erroneous than satellite-based data over irrigated areas.

- 4) Finally, we illustrated that selective use of satellite and model data dramatically improves the quality of SSM data.

## 5. Conclusions

The purpose of this study was to analyze global-scale SSM error characteristics with regard to the degree of dense vegetation and irrigation, using both satellite and model-based SSM estimates. First, we focused on the performance of the satellite- and model-based SSM data globally, then over areas generally regarded as problematic (i.e., forest and irrigated regions). Forest regions are considered problematic for remote sensing SSM estimates, as the vegetation layer attenuates the soil signal (the attenuation effects increasing with frequency), while irrigated regions are considered as problematic for model-based SSM products as irrigated land is too heterogeneous at the scale of current satellites.

Since high-density ground-based SSM networks are limited in space, methods of cross-comparing two or three independent collocated SSM data sets have recently been developed for evaluating SSM model/retrieval errors on a global scale. The error characteristics of four different satellites and two model-based products were intercompared using TCA and ground SM measurements. We were able to provide new insights into the advantages and disadvantages of current satellite and

model-based SSM products focused on forest and irrigated areas. We also showed that the choice of triplets for TCA can have a dramatic impact on the final results.

Even though satellite and model-based SSM estimates showed a similar spatial pattern on a global scale, the TCA results showed very different error patterns with regard to SSM. Interestingly, satellite-based SSM products performed well in predicting SSM over areas of high vegetation matter (to the exception of dense tropical forests) and also they showed high potential for predicting SSM in areas where unexpected signals caused by artificial changes to the land surface (i.e., irrigated areas) make prediction of SSM difficult for land surface models. In addition, ERA5 seems to include irrigation schemes through the assimilation of ASCAT SSM data. We discovered that no products we analyzed showed obvious degradation in TCA-based errors under different vegetated conditions; however, the degradation of both satellite and model data over irrigated areas is more obvious. The degradation of SMOS is likely due to RFI in India and China.

Selectively using multi-source SSM data according to the TCA results, we were able to obtain a SSM data set with the highest signal-to-noise ratio. This encouraging result indicates that global-scale, high-quality SSM data sets over the forest and irrigated lands — long considered difficult regions for estimating SSM by either satellite observation or modeling techniques — can be obtained through a combination of satellite and model data sets. However, selective use of satellite data set still included some limitations over densely forested and actively irrigated areas such as China and central Africa.

In this study, we only considered SSM products at a spatial

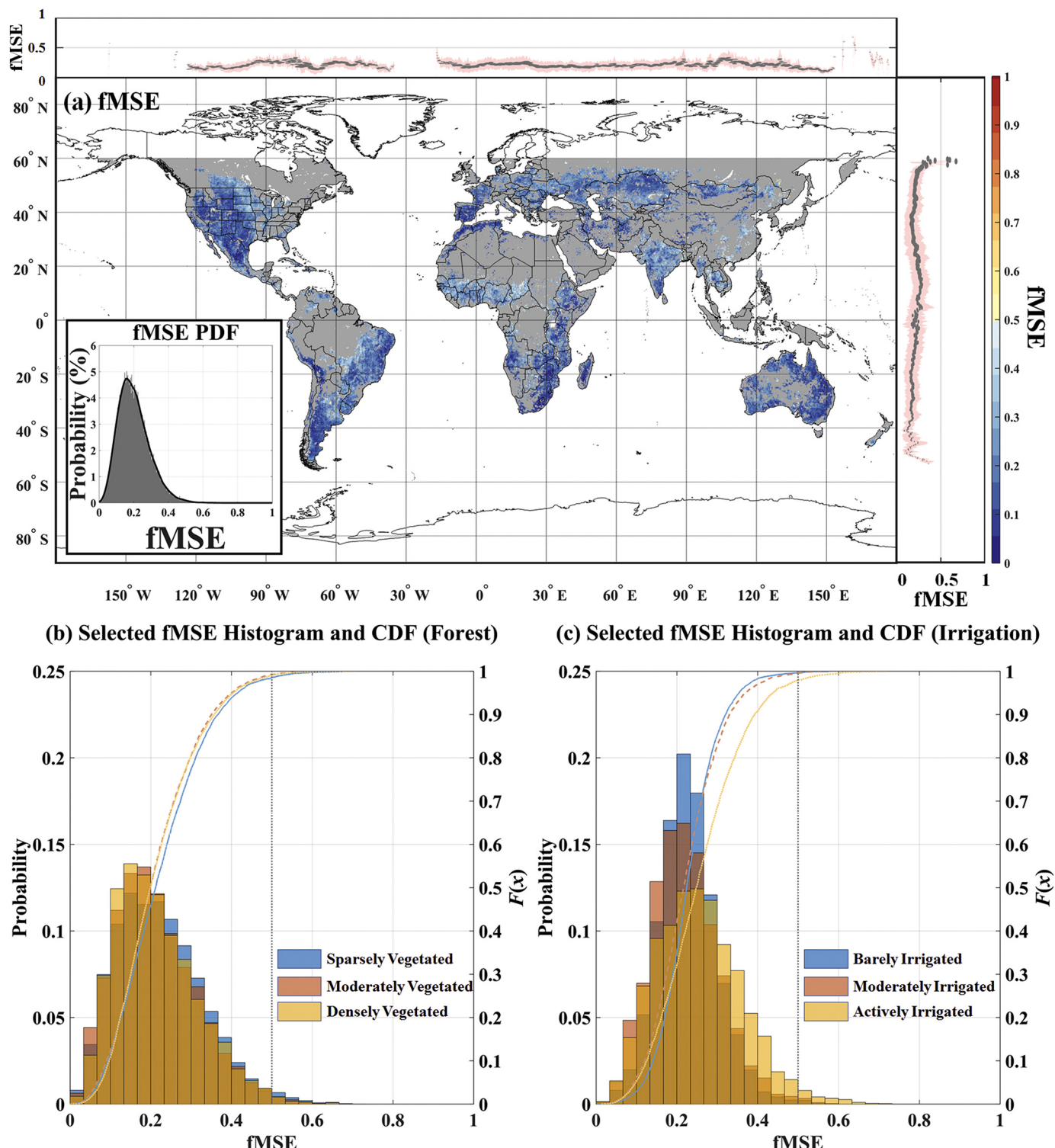


**Fig. 10.** (a) Map of fMSE of combined data. Upper and right panels indicate longitude and latitude zonal means of fMSE, respectively. Inset graphs represent PDF, marker sizes in zonal plots illustrate proportional to zonal land areas, and the shaded region shows  $\pm 1$  standard deviation. (b) Probability histogram and CDF of fMSE values for combined data over sparsely vegetated regions (blue bars and lines), moderately vegetated regions (red bars and lines), and densely vegetated regions (yellow bars and lines). (c) Probability histogram and CDF of fMSE values for combined data over barely irrigated areas (blue bars and lines), moderately irrigated areas (red bars and lines), and actively irrigated areas (yellow bars and lines). (For interpretation of the references to colour in this figure legend, the reader is referred to the web version of this article.)

resolution of 0.25 degrees. Future investigation of the sensitivity of spatial resolution to irrigation impact will require higher spatial resolution data from satellite and model-based SSM in order to account for the heterogeneity of intracellular processes within a 0.25-degree

resolution gridcell. Currently, SMAP/Sentinel combined and Sentinel-1 SSM data are available (Das et al., 2019; Bauer-Marschallinger et al., 2018); however, no 1-km SMOS or AMSR2 data are publicly available on a global scale. Even if such products become available in the near

future, obtaining a TCA for these products would be challenging since downscaled SSM products are mostly a combination of different band range products, and sharing similar ancillary data such as vegetation or temperature data from the Moderate Resolution Imaging Spectroradiometer (MODIS) or LSMs would violate the assumptions of TCA. Furthermore, we only considered specific versions of satellite and model-based data sets. Therefore, for instance, the SMOS data set based on the original Level 2 algorithm distributed by Centre Aval de Traitement des Données SMOS (CATDS) may behave differently than the SMOS-IC data used in this study. Updated and alternate choices for satellite-based SSM and model-based data sets can be utilized in future research; thus, spatial and temporal coverage having higher-quality SSM estimates can be obtained over the areas which current research is unable to access.

Many other factors also affect the estimation of error characteristics in model-based SSM data, including poor quality forcing data in GLDAS (and ERA5), representative depth differences, selection of triplets, etc. These factors may cause biased results in characterizing model-based SM errors. In this study, we explicitly and implicitly showed that TCA results can be biased if the triplets are poorly selected. It was demonstrated that the depth mismatch between satellites (e.g., 5-cm SM from SMAP) and model-based data (e.g., 10-cm SM from GLDAS) can lead to biased TCA-based numbers because of the nonorthogonal errors. Furthermore, results from TCA with non-mutually independent triplets will result in over graded/under graded performance of the individual product.

Finally, further analysis will be required in future studies, using higher spatial and temporal resolution SSM data from satellite data, as satellite footprints and temporal repeat might not fine enough to capture the irrigation signals. The new data sets for SSM from Cyclone Global Navigation Satellite System (CYGNSS) and the downscaled SSM from passive and active systems can be used for better spatial resolutions and temporal repeat characterization of the land surface state. The new data sets for SSM from CYGNSS (Kim and Lakshmi, 2018) and the downscaled SSM from passive radiometers (Das et al., 2019; Fang et al., 2018; Narayan and Lakshmi, 2008) can be used for better spatial resolutions and temporal repeat characterization of the land surface state. In addition, we only investigated the error characteristics of surface-level SM; however, TCA for large-scale RZSM data, such as the Global Land Evaporation Amsterdam Model (GLEAM) RZSM and SMAP L4 data are also important in understanding land-atmospheric feedback and improving hydrologic forecasting (Crow et al., 2017; Dong et al., 2019a; Lakshmi et al., 2011; Martens et al., 2017; Matsui and Lakshmi, 2003; Reichle et al., 2017).

#### Disclaimer

Any use of trade, firm, or product names is for descriptive purposes only and does not imply endorsement by the US Government.

#### Declaration of competing interest

The authors declare that they have no known competing financial interests or personal relationships that could have appeared to influence the work reported in this paper.

#### Acknowledgments

We gratefully acknowledge funding from the NASA Terrestrial Hydrology Program (Program Manager Dr. Jared Entin, Grant # NNX12AP75G). The authors thank the teams from NASA, USGS, USGS, ESA, and JAXA for making their data sets publicly available. Hyunglok Kim acknowledges the Future Investigators in NASA Earth and Space Science and Technology (FINESST) under Award #80NSSC19K1337" and the Bicentennial Fellowship from the Department of Engineering Systems and Environment at the University of Virginia. USDA is an equal opportunity employer and provider. This research was a

contribution from the Long-Term Agroecosystem Research (LTAR) network. LTAR is supported by the United States Department of Agriculture. The most recent SMOS-IC soil moisture data were personally provided by Mr. Xiaojun Li.

#### Appendix A. Supplementary data

Supplementary data to this article can be found online at <https://doi.org/10.1016/j.rse.2020.112052>.

#### References

- Abolafia-Rosenzweig, R., Livneh, B., Small, E.E., Kumar, S.V., 2019. Soil moisture data assimilation to estimate irrigation water use. *J. Adv. Model. Earth Syst.* 11, 3670–3690. <https://doi.org/10.1029/2019MS001797>.
- Alemohammad, S.H., McColl, K.A., Konings, A.G., Entekhabi, D., Stoffelen, A., 2015. Characterization of precipitation product errors across the United States using multiplicative triple collocation. *Hydrol. Earth Syst. Sci.* 19, 3489–3503. <https://doi.org/10.5194/hess-19-3489-2015>.
- Al-Yaari, A., Wigneron, J.-P., Ducharme, A., Kerr, Y., de Rosnay, P., de Jeu, R., Govind, A., Al Bitar, A., Albergel, C., Muñoz-Sabater, J., Richaume, P., Mialon, A., 2014a. Global-scale evaluation of two satellite-based passive microwave soil moisture datasets (SMOS and AMSR-E) with respect to Land Data Assimilation System estimates. *Remote Sens. Environ.* 149, 181–195. <https://doi.org/10.1016/j.rse.2014.04.006>.
- Al-Yaari, A., Wigneron, J.-P., Ducharme, A., Kerr, Y.H., Wagner, W., De Lannoy, G., Reichle, R., Al Bitar, A., Dorigo, W., Richaume, P., Mialon, A., 2014b. Global-scale comparison of passive (SMOS) and active (ASCAT) satellite-based microwave soil moisture retrievals with soil moisture simulations (MERRA-land). *Remote Sens. Environ.* 152, 614–626. <https://doi.org/10.1016/j.rse.2014.07.013>.
- Al-Yaari, A., Ducharme, A., Cheruy, F., Crow, W.T., Wigneron, J.-P., 2019a. Satellite-based soil moisture provides missing link between summertime precipitation and surface temperature biases in CMIP5 simulations over conterminous United States. *Sci. Rep.* 9, 1657. <https://doi.org/10.1038/s41598-018-38309-5>.
- Al-Yaari, A., Wigneron, J.-P., Dorigo, W., Colliander, A., Pellarin, T., Hahn, S., Mialon, A., Richaume, P., Fernandez-Moran, R., Fan, L., Kerr, Y.H., De Lannoy, G., 2019b. Assessment and inter-comparison of recently developed/reprocessed microwave satellite soil moisture products using ISMN ground-based measurements. *Remote Sens. Environ.* 224, 289–303. <https://doi.org/10.1016/j.rse.2019.02.008>.
- Anderson, M.C., Norman, J.M., Mecikalski, J.R., Otkin, J.A., Kustas, W.P., 2007. A climatological study of evapotranspiration and moisture stress across the continental United States based on thermal remote sensing: 1. Model formulation: EVAPOTRANSPIRATION AND MOISTURE STRESS. *J. Geophys. Res.* 112. <https://doi.org/10.1029/2006JD007506>.
- Bauer-Marschallinger, B., Freeman, V., Cao, S., Paulik, C., Schaufler, S., Stachl, T., ... Wagner, W., 2018. Toward global soil moisture monitoring with Sentinel-1: Harnessing assets and overcoming obstacles. *IEEE Transactions on Geoscience and Remote Sensing* 57 (1), 520–539.
- Beck, H.E., Pan, M., Miralles, D.G., Reichle, R.H., Dorigo, W.A., Hahn, S., Sheffield, J., Karthikeyan, L., Balsamo, G., Parinussa, R.M., van Dijk, A.I.J.M., Du, J., Kimball, J.S., Vergopolan, N., Wood, E.F., 2020. Evaluation of 18 satellite- and model-based soil moisture products using in situ measurements from 826 sensors (preprint). *Global Hydrol. Model. Approach*. <https://doi.org/10.5194/hess-2020-184>.
- Bindlish, R., Jackson, T., Cosh, M., Zhao, T., O'Neill, P., 2015. Global soil moisture from the aquarius/SAC-D satellite: description and initial assessment. *IEEE Geosci. Remote Sens. Lett.* 12, 923–927. <https://doi.org/10.1109/LGRS.2014.2364151>.
- Bindlish, R., Cosh, M.H., Jackson, T.J., Koike, T., Fujii, H., Chan, S.K., Asanuma, J., Berg, A., Bosch, D.D., Caldwell, T., Collins, C.H., McNairn, H., Martínez-Fernández, J., Prueger, J., Rowlandson, T., Seyfried, M., Starks, P., Thibeault, M., Velde, R.V.D., Walker, J.P., Coopersmith, E.J., 2018. GCOM-W AMSR2 soil moisture product validation using core validation sites. *IEEE J. Sel. Top. Appl. Earth Obs. Remote Sens.* 11, 209–219. <https://doi.org/10.1109/JSTARS.2017.2754293>.
- Brocca, L., Hasenauer, S., Lacava, T., Melone, F., Moramarco, T., Wagner, W., Dorigo, W., Matgen, P., Martínez-Fernández, J., Llorens, P., Latron, J., Martin, C., Bittelli, M., 2011. Soil moisture estimation through ASCAT and AMSR-E sensors: an inter-comparison and validation study across Europe. *Remote Sens. Environ.* 115, 3390–3408. <https://doi.org/10.1016/j.rse.2011.08.003>.
- Brocca, L., Filippucci, P., Hahn, S., Ciabatta, L., Massari, C., Camici, S., Schüller, L., Bojkov, B., Wagner, W., 2019. SM2RAIN-ASCAT (2007–2018): global daily satellite rainfall data from ASCAT soil moisture observations. *Earth Syst. Sci. Data* 11, 1583–1601. <https://doi.org/10.5194/essd-11-1583-2019>.
- Burgin, M.S., Colliander, A., Njoku, E.G., Chan, S.K., Cabot, F., Kerr, Y.H., Bindlish, R., Jackson, T.J., Entekhabi, D., Yueh, S.H., 2017. A comparative study of the SMAP passive soil moisture product with existing satellite-based soil moisture products. *IEEE Trans. Geosci. Remote Sens.* 55, 2959–2971. <https://doi.org/10.1109/TGRS.2017.2656859>.
- Caires, S., 2003. Validation of ocean wind and wave data using triple collocation. *J. Geophys. Res.* 108, 3098. <https://doi.org/10.1029/2002JC001491>.
- Chapin, E., Chau, A., Chen, J., Heavey, B., Hensley, S., Lou, Y., Machuzak, R., Moghaddam, M., 2012. AirMOSS: An airborne P-band SAR to measure root-zone soil moisture. In: 2012 IEEE Radar Conference. IEEE, Atlanta, GA, pp. 0693–0698. <https://doi.org/10.1109/RADAR.2012.6212227>. Presented at the 2012 IEEE Radar Conference (RadarCon).

- Chen, F., Crow, W.T., Colliander, A., Cosh, M.H., Jackson, T.J., Bindlish, R., Reichle, R.H., Chan, S.K., Bosch, D.D., Starks, P.J., Goodrich, D.C., Seyfried, M.S., 2017. Application of triple collocation in ground-based validation of soil moisture active/passive (SMAP) level 2 data products. *IEEE J. Sel. Top. Appl. Earth Obs. Remote Sens.* 10, 489–502. <https://doi.org/10.1109/JSTARS.2016.2569998>.
- Chen, F., Crow, W.T., Bindlish, R., Colliander, A., Burgin, M.S., Asanuma, J., Aida, K., 2018. Global-scale evaluation of SMAP, SMOS and ASCAT soil moisture products using triple collocation. *Remote Sens. Environ.* 214, 1–13. <https://doi.org/10.1016/j.rse.2018.05.008>.
- Cho, E., Moon, H., Choi, M., 2015. First assessment of the advanced microwave scanning radiometer 2 (AMSR2) soil moisture contents in Northeast Asia. *J. Meteorol. Soc. Jpn.* 93, 117–129. <https://doi.org/10.2151/jmsj.2015-008>.
- Cho, E., Jacobs, J.M., Jia, X., Kraatz, S., 2019. Identifying subsurface drainage using satellite big data and machine learning via Google earth engine. *Water Resour. Res.* 55, 8028–8045. <https://doi.org/10.1029/2019WR024892>.
- Colliander, A., Cosh, M.H., Misra, S., Jackson, T.J., Crow, W.T., Chan, S., Bindlish, R., Chae, C., Holifield Collins, C., Yueh, S.H., 2017. Validation and scaling of soil moisture in a semi-arid environment: SMAP validation experiment 2015 (SMAPVEX15). *Remote Sens. Environ.* 196, 101–112. <https://doi.org/10.1016/j.rse.2017.04.022>.
- Cook, B.I., Puma, M.J., Krakauer, N.Y., 2011. Irrigation induced surface cooling in the context of modern and increased greenhouse gas forcing. *Clim. Dyn.* 37, 1587–1600. <https://doi.org/10.1007/s00382-010-0932-x>.
- Costa, M.H., Souza-Filho, J.C., Ribeiro, A., 2004. Comments on “The Regional Evapotranspiration of the Amazon”. *J. Hydrometeorol.* 5, 1279–1280. <https://doi.org/10.1175/JHM-393.1>.
- Cox, P.M., Betts, R.A., Jones, C.D., Spall, S.A., Totterdell, I.J., 2000. Acceleration of global warming due to carbon-cycle feedbacks in a coupled climate model. *Nature* 408, 184–187. <https://doi.org/10.1038/35041539>.
- Crow, W.T., Bindlish, R., Jackson, T.J., 2005. The added value of spaceborne passive microwave soil moisture retrievals for forecasting rainfall-runoff partitioning: VALUE OF SPACEBORNE SOIL MOISTURE. *Geophys. Res. Lett.* 32. <https://doi.org/10.1029/2005GL023543>.
- Crow, W.T., Berg, A.A., Cosh, M.H., Loew, A., Mohanty, B.P., Panciera, R., de Rosnay, P., Ryu, D., Walker, J.P., 2012. Upscaling sparse ground-based soil moisture observations for the validation of coarse-resolution satellite soil moisture products. *Rev. Geophys.* 50. <https://doi.org/10.1029/2011RG000372>.
- Crow, W.T., Chen, F., Reichle, R.H., Liu, Q., 2017. L band microwave remote sensing and land data assimilation improve the representation of prestorm soil moisture conditions for hydrologic forecasting: estimation of prestorm soil moisture. *Geophys. Res. Lett.* 44, 5495–5503. <https://doi.org/10.1002/2017GL073642>.
- Das, N.N., Mohanty, B.P., 2006. Root zone soil moisture assessment using remote sensing and vadose zone modeling. *Vadose Zone J.* 5 (1), 296–307. <https://doi.org/10.2136/vzj2005.0033>.
- Das, N.N., Entekhabi, D., Dunbar, R.S., Chaubell, M.J., Colliander, A., Yueh, S., Jagdhuber, T., Chen, F., Crow, W., O’Neill, P.E., Walker, J.P., Berg, A., Bosch, D.D., Caldwell, T., Cosh, M.H., Collins, C.H., Lopez-Baeza, E., Thibault, M., 2019. The SMAP and Copernicus sentinel 1A/B microwave active-passive high resolution surface soil moisture product. *Remote Sens. Environ.* 233, 111380. <https://doi.org/10.1016/j.rse.2019.111380>.
- Deines, J.M., Kendall, A.D., Hyndman, D.W., 2017. Annual irrigation dynamics in the U.S. northern high plains derived from Landsat satellite data: satellite-derived irrigation dynamics. *Geophys. Res. Lett.* 44, 9350–9360. <https://doi.org/10.1002/2017GL074071>.
- Ding, Q., Steig, E.J., Battisti, D.S., Küttel, M., 2011. Winter warming in West Antarctica caused by central tropical Pacific warming. *Nat. Geosci.* 4, 398–403. <https://doi.org/10.1038/geo1129>.
- Dong, J., Crow, W.T., 2017. An improved triple collocation analysis algorithm for decomposing autocorrelated and white soil moisture retrieval errors: OBSERVATION ERROR DECOMPOSITION. *J. Geophys. Res. Atmos.* 122, 13,081–13,094. <https://doi.org/10.1002/2017JD027387>.
- Dong, J., Crow, W.T., 2018. The added value of assimilating remotely sensed soil moisture for estimating summertime soil moisture-air temperature coupling strength. *Water Resour. Res.* 54, 6072–6084. <https://doi.org/10.1029/2018WR022619>.
- Dong, J., Crow, W.T., Bindlish, R., 2018. The error structure of the SMAP single and dual channel soil moisture retrievals. *Geophys. Res. Lett.* 45, 758–765. <https://doi.org/10.1002/2017GL075656>.
- Dong, J., Crow, W., Reichle, R., Liu, Q., Lei, F., Cosh, M.H., 2019a. A global assessment of added value in the SMAP level 4 soil moisture product relative to its baseline land surface model. *Geophys. Res. Lett.* 46, 6604–6613. <https://doi.org/10.1029/2019GL083398>.
- Dong, J., Crow, W.T., Duan, Z., Wei, L., Lu, Y., 2019b. A double instrumental variable method for geophysical product error estimation. *Remote Sens. Environ.* 225, 217–228. <https://doi.org/10.1016/j.rse.2019.03.003>.
- Dong, J., Crow, W.T., Tobin, K.J., Cosh, M.H., Bosch, D.D., Starks, P.J., Seyfried, M., Collins, C.H., 2020. Comparison of microwave remote sensing and land surface modeling for surface soil moisture climatology estimation. *Remote Sens. Environ.* 242, 111756. <https://doi.org/10.1016/j.rse.2020.111756>.
- Dorigo, W.A., Wagner, W., Hohensinn, R., Hahn, S., Paulik, C., Xaver, A., Gruber, A., Drusch, M., Mecklenburg, S., van Oevelen, P., Robock, A., Jackson, T., 2011. The International Soil Moisture Network: a data hosting facility for global in situ soil moisture measurements. *Hydrol. Earth Syst. Sci.* 15, 1675–1698. <https://doi.org/10.5194/hess-15-1675-2011>.
- Dorigo, W.A., Xaver, A., Vreugdenhil, M., Gruber, A., Hegyiiová, A., Sanchis-Dufau, A.D., Zamojski, D., Cordes, C., Wagner, W., Drusch, M., 2013. Global automated quality control of in situ soil moisture data from the international soil moisture network. *Vadose Zone J.* 12. <https://doi.org/10.2136/vzj2012.0097>.
- Dorigo, W.A., Gruber, A., De Jeu, R.A.M., Wagner, W., Stacke, T., Loew, A., Albergel, C., Brocca, L., Chung, D., Parinussa, R.M., Kidd, R., 2015. Evaluation of the ESA CCI soil moisture product using ground-based observations. *Remote Sens. Environ.* 162, 380–395. <https://doi.org/10.1016/j.rse.2014.07.023>.
- Dorigo, W., Wagner, W., Albergel, C., Albrecht, F., Balsamo, G., Brocca, L., Chung, D., Ertl, M., Forkel, M., Gruber, A., Haas, E., Hamer, P.D., Hirschi, M., Ikonen, J., de Jeu, R., Kidd, R., Lahoz, W., Liu, Y.Y., Miralles, D., Mistelbauer, T., Nicolai-Shaw, N., Parinussa, R., Pratola, C., Reimer, C., van der Schalie, R., Seneviratne, S.I., Smolander, T., Lecomte, P., 2017. ESA CCI soil moisture for improved earth system understanding: state-of-the art and future directions. *Remote Sens. Environ.* 203, 185–215. <https://doi.org/10.1016/j.rse.2017.07.001>.
- Draper, C., Reichle, R., de Jeu, R., Naemici, V., Parinussa, R., Wagner, W., 2013. Estimating root mean square errors in remotely sensed soil moisture over continental scale domains. *Remote Sens. Environ.* 137, 288–298. <https://doi.org/10.1016/j.rse.2013.06.013>.
- Dumedah, G., Walker, J.P., Merlin, O., 2015. Root-zone soil moisture estimation from assimilation of down-scaled soil moisture and ocean salinity data. *Adv. Water Resour.* 84, 14–22. <https://doi.org/10.1016/j.advwatres.2015.07.021>.
- Entekhabi, D., Njoku, E.G., O'Neill, P.E., Kellogg, K.H., Crow, W.T., Edelstein, W.N., Entin, J.K., Goodman, S.D., Jackson, T.J., Johnson, J., Kimball, J., Piepmeyer, J.R., Koster, R.D., Martin, N., McDonald, K.C., Moghaddam, M., Moran, S., Reichle, R., Shi, J.C., Spencer, M.W., Thurman, S.W., Tsang, L., Zyl, J.V., 2010. The soil moisture active passive (SMAP) mission. *Proc. IEEE* 98, 704–716. <https://doi.org/10.1109/JPROC.2010.2043918>.
- Escorihuela, M.J., Quintana-Seguí, P., 2016. Comparison of remote sensing and simulated soil moisture datasets in Mediterranean landscapes. *Remote Sens. Environ.* 180, 99–114. <https://doi.org/10.1016/j.rse.2016.02.046>.
- Fang, B., Lakshmi, V., Bindlish, R., Jackson, T.J., 2018. Downscaling of SMAP soil moisture using land surface temperature and vegetation data. *Vadose Zone J.* 17, 170198. <https://doi.org/10.2136/vzj2017.11.0198>.
- Fernandez-Moran, R., Al-Yaari, A., Mialon, A., Mahmoodi, A., Al Bitar, A., De Lannoy, G., Rodriguez-Fernandez, N., Lopez-Baeza, E., Kerr, Y., Wigneron, J.-P., 2017. SMOS-IC: an alternative SMOS soil moisture and vegetation optical depth product. *Remote Sens.* 9, 457. <https://doi.org/10.3390/rs9050457>.
- Ford, T.W., Harris, E., Quiring, S.M., 2014. Estimating root zone soil moisture using near-surface observations from SMOS. *Hydrol. Earth Syst. Sci.* 18, 139–154. <https://doi.org/10.5194/hess-18-139-2014>.
- Frison, P.L., Mougin, E., 1996. Monitoring global vegetation dynamics with ERS-1 wind scatterometer data. *Int. J. Remote Sens.* 17, 3201–3218. <https://doi.org/10.1080/01431169608949139>.
- Gruber, A., Su, C.-H., Zwieback, S., Crow, W., Dorigo, W., Wagner, W., 2016. Recent advances in (soil moisture) triple collocation analysis. *Int. J. Appl. Earth Obs. Geoinf.* 45, 200–211. <https://doi.org/10.1016/j.jag.2015.09.002>.
- Gruber, A., Dorigo, W.A., Crow, W., Wagner, W., 2017. Triple collocation-based merging of satellite soil moisture retrievals. *IEEE Trans. Geosci. Remote Sens.* 55, 6780–6792. <https://doi.org/10.1109/TGRS.2017.2734070>.
- Jackson, T.J., Cosh, M.H., Bindlish, R., Starks, P.J., Bosch, D.D., Seyfried, M., Goodrich, D.C., Moran, M.S., Du, J., 2010. Validation of advanced microwave scanning radiometer soil moisture products. *IEEE Trans. Geosci. Remote Sens.* 48, 4256–4272. <https://doi.org/10.1109/TGRS.2010.2051035>.
- Juárez, R.I.N., Hodnett, M.G., Fu, R., Goulden, M.L., von Randow, C., 2007. Control of dry season evapotranspiration over the Amazonian Forest as inferred from observations at a southern Amazon Forest site. *J. Clim.* 20, 2827–2839. <https://doi.org/10.1175/JCLI4184.1>.
- Karthikeyan, L., Pan, M., Wanders, N., Kumar, D.N., Wood, E.F., 2017. Four decades of microwave satellite soil moisture observations: Part 1. A review of retrieval algorithms. *Adv. Water Resour.* 109, 106–120. <https://doi.org/10.1016/j.advwatres.2017.09.006>.
- Kerr, Y.H., Waldteufel, P., Wigneron, J., Martinuzzi, J., Font, J., Berger, M., 2001. Soil moisture retrieval from space: the Soil Moisture and Ocean Salinity (SMOS) mission. *IEEE Trans. Geosci. Remote Sens.* 39, 1729–1735. <https://doi.org/10.1109/36.942551>.
- Khan, M.S., Liaqat, U.W., Baik, J., Choi, M., 2018. Stand-alone uncertainty characterization of GLEAM, GLDAS and MOD16 evapotranspiration products using an extended triple collocation approach. *Agric. For. Meteorol.* 252, 256–268. <https://doi.org/10.1016/j.agrformet.2018.01.022>.
- Kim, H., Lakshmi, V., 2018. Use of cyclone global navigation satellite system (cygnss) observations for estimation of soil moisture. *Geophys. Res. Lett.* 45, 8272–8282. <https://doi.org/10.1029/2018GL078923>.
- Kim, H., Lakshmi, V., 2019. Global dynamics of stored precipitation water in the topsoil layer from satellite and reanalysis data. *Water Resour. Res.* 55, 3328–3346. <https://doi.org/10.1029/2018WR023166>.
- Kim, H., Parinussa, R., Konings, A.G., Wagner, W., Cosh, M.H., Lakshmi, V., Zohaib, M., Choi, M., 2018. Global-scale assessment and combination of SMAP with ASCAT (active) and AMSR2 (passive) soil moisture products. *Remote Sens. Environ.* 204, 260–275. <https://doi.org/10.1016/j.rse.2017.10.026>.
- Kim, H., Cosh, M.H., Bindlish, R., Lakshmi, V., 2020. Field evaluation of portable soil water content sensors in a sandy loam. *Vadose Zone J.* 19. <https://doi.org/10.1002/vzj2.20033>.
- Konings, A.G., Entekhabi, D., Chan, S.K., Njoku, E.G., 2011. Effect of radiative transfer uncertainty on L-band radiometric soil moisture retrieval. *IEEE Trans. Geosci. Remote Sens.* 49, 2686–2698. <https://doi.org/10.1109/TGRS.2011.2105495>.
- Konings, A.G., Piles, M., Das, N., Entekhabi, D., 2017. L-band vegetation optical depth and effective scattering albedo estimation from SMAP. *Remote Sens. Environ.* 198, 460–470. <https://doi.org/10.1016/j.rse.2017.06.037>.

- Kumar, S., Peterslidard, C., Tian, Y., Houser, P., Geiger, J., Olden, S., Lighty, L., Eastman, J., Doty, B., Dirmeyer, P., 2006. Land information system: an interoperable framework for high resolution land surface modeling. *Environ. Model. Softw.* 21, 1402–1415. <https://doi.org/10.1016/j.envsoft.2005.07.004>.
- Kumar, S.V., Peters-Lidard, C.D., Santanello, J.A., Reichle, R.H., Draper, C.S., Koster, R.D., Nearing, G., Jasinski, M.F., 2015. Evaluating the utility of satellite soil moisture retrievals over irrigated areas and the ability of land data assimilation methods to correct for unmodeled processes. *Hydrol. Earth Syst. Sci.* 19, 4463–4478. <https://doi.org/10.5194/hess-19-4463-2015>.
- Lakshmi, V., Wood, E.F., Choudhury, B.J., 1997. Evaluation of special sensor microwave/imager satellite data for regional soil moisture estimation over the Red River Basin. *J. Appl. Meteorol.* 36, 20.
- Lakshmi, V., Hong, S., Small, E.E., Chen, F., 2011. The influence of the land surface on hydroclimate and ecology: new advances from modeling and satellite remote sensing. *Hydrolog. Res.* 42, 95–112. <https://doi.org/10.2166/nh.2011.071>.
- Lawston, P.M., Santanello, J.A., Kumar, S.V., 2017. Irrigation signals detected from SMAP soil moisture retrievals: irrigation signals detected from SMAP. *Geophys. Res. Lett.* 44, 11,860–11,867. <https://doi.org/10.1002/2017GL075733>.
- Li, X., Al-Yaari, A., Schwank, M., Fan, L., Frappart, F., Swenson, J., Wigneron, J.-P., 2020. Compared performances of SMOS-IC soil moisture and vegetation optical depth retrievals based on Tau-Omega and Two-Stream microwave emission models. *Remote Sens. Environ.* 236, 111502. <https://doi.org/10.1016/j.rse.2019.111502>.
- Lo, M.-H., Famiglietti, J.S., 2013. Irrigation in California's Central Valley strengthens the southwestern U.S. water cycle: CENTRAL VALLEY IRRIGATION STRENGTHENS U.S. MONSOON. *Geophys. Res. Lett.* 40, 301–306. <https://doi.org/10.1002/grl.50108>.
- Lobell, D., Bala, G., Mirin, A., Phillips, T., Maxwell, R., Rotman, D., 2009. Regional differences in the influence of irrigation on climate. *J. Clim.* 22, 2248–2255. <https://doi.org/10.1175/2008JCLI2703.1>.
- Ma, H., Zeng, J., Chen, N., Zhang, X., Cosh, M.H., Wang, W., 2019. Satellite surface soil moisture from SMAP, SMOS, AMSR2 and ESA CCI: a comprehensive assessment using global ground-based observations. *Remote Sens. Environ.* 231, 111215. <https://doi.org/10.1016/j.rse.2019.111215>.
- Martens, B., Miralles, D.G., Lievens, H., van der Schalie, R., de Jeu, R.A.M., Fernández-Prieto, D., Beck, H.E., Dorigo, W.A., Verhoest, N.E.C., 2017. GLEAM v3: satellite-based land evaporation and root-zone soil moisture. *Geosci. Model Dev.* 10, 1903–1925. <https://doi.org/10.5194/gmd-10-1903-2017>.
- Matsui, T., Lakshmi, V., 2003. Links between snow cover, surface skin temperature, and rainfall variability in the North American monsoon system. *J. Clim.* 16, 9.
- McColl, K.A., Vogelzang, J., Konings, A.G., Entekhabi, D., Piles, M., Stoffelen, A., 2014. Extended triple collocation: estimating errors and correlation coefficients with respect to an unknown target. *Geophys. Res. Lett.* 41, 6229–6236. <https://doi.org/10.1002/2014GL061322>.
- Miyaoka, K., Gruber, A., Ticconi, F., Hahn, S., Wagner, W., Figa-Saldana, J., Anderson, C., 2017. Triple collocation analysis of soil moisture from Metop-A ASCAT and SMOS against JRA-55 and ERA-Interim. *IEEE J. Sel. Top. Appl. Earth Obs. Remote Sens.* 10, 2274–2284. <https://doi.org/10.1109/JSTARS.2016.2632306>.
- Morrison, K., Wagner, W., 2019. Explaining anomalies in SAR and scatterometer soil moisture retrievals from dry soils with subsurface scattering. *IEEE Trans. Geosci. Remote Sensing* 1–8. <https://doi.org/10.1109/TGRS.2019.2954771>.
- Narayan, U., Lakshmi, V., 2008. Characterizing subpixel variability of low resolution radiometer derived soil moisture using high resolution radar data: CHARAC. SUBPIXEL V. *Water Resour. Res.* 44. <https://doi.org/10.1029/2006WR005817>.
- Nguyen, H.H., Kim, H., Choi, M., 2017. Evaluation of the soil water content using cosmic-ray neutron probe in a heterogeneous monsoon climate-dominated region. *Adv. Water Resour.* 108, 125–138. <https://doi.org/10.1016/j.advwatres.2017.07.020>.
- O'Neill, P., Chan, S., Njoku, E., Jackson, T., & Bindlish, R. (2015). Soil moisture active passive (SMAP) algorithm theoretical basis document Level 2 & 3 soil moisture (passive) data products. Jet Propulsion Laboratory, NASA: Pasadena, CA, USA.
- Owe, M., de Jeu, R., Walker, J., 2001. A methodology for surface soil moisture and vegetation optical depth retrieval using the microwave polarization difference index. *IEEE Trans. Geosci. Remote Sens.* 39, 1643–1654. <https://doi.org/10.1109/36.942542>.
- Pei, L., Moore, N., Zhong, S., Kendall, A.D., Gao, Z., Hyndman, D.W., 2016. Effects of irrigation on summer precipitation over the United States. *J. Clim.* 29, 3541–3558. <https://doi.org/10.1175/JCLI-D-15-0337.1>.
- Pryor, S.C., Sullivan, R.C., Wright, T., 2016. Quantifying the roles of changing albedo, emissivity, and energy partitioning in the impact of irrigation on atmospheric heat content. *J. Appl. Meteorol. Climatol.* 55, 1699–1706. <https://doi.org/10.1175/JAMC-D-15-0291.1>.
- Puma, M.J., Cook, B.I., 2010. Effects of irrigation on global climate during the 20th century. *J. Geophys. Res.* 115, D16120. <https://doi.org/10.1029/2010JD014122>.
- Reichle, R.H., De Lannoy, G.J.M., Liu, Q., Ardizzone, J.V., Colliander, A., Conaty, A., Crow, W., Jackson, T.J., Jones, L.A., Kimball, J.S., Koster, R.D., Mahanama, S.P., Smith, E.B., Berg, A., Bircher, S., Bosch, D., Caldwell, T.G., Cosh, M., González-Zamora, Á., Holifield Collins, C.D., Jensen, K.H., Livingston, S., Lopez-Baeza, E., Martínez-Fernández, J., McNairn, H., Moghaddam, M., Pacheco, A., Pellarin, T., Prueger, J., Rowlandson, T., Seyfried, M., Stark, P., Su, Z., Thibeault, M., van der Velde, R., Walker, J., Wu, X., Zeng, Y., 2017. Assessment of the SMAP Level-4 surface and root-zone soil moisture product using in situ measurements. *J. Hydrometeorol.* 18, 2621–2645. <https://doi.org/10.1175/JHM-D-17-0063.1>.
- Rodell, M., Houser, P.R., Jambor, U., Gottschalck, J., Mitchell, K., Meng, C.-J., Arsenault, K., Cosgrove, B., Radakovich, J., Bosilovich, M., Entin, J.K., Walker, J.P., Lohmann, D., Toll, D., 2004. The global land data assimilation system. *Bull. Amer. Meteor. Soc.* 85, 381–394. <https://doi.org/10.1175/BAMS-85-3-381>.
- Sacks, W.J., Cook, B.I., Buenning, N., Lewis, S., Helkowski, J.H., 2009. Effects of global irrigation on the near-surface climate. *Clim. Dyn.* 33, 159–175. <https://doi.org/10.1007/s00382-008-0445-z>.
- Sadeghi, M., Gao, L., Ebtehaj, A., Wigneron, J.-P., Crow, W.T., Reager, J.T., Warrick, A.W., 2020. Retrieving global surface soil moisture from GRACE satellite gravity data. *J. Hydrol.* 584, 124717. <https://doi.org/10.1016/j.jhydrol.2020.124717>.
- Salmon, J.M., Friedl, M.A., Frolking, S., Wisser, D., Douglas, E.M., 2015. Global rain-fed, irrigated, and paddy croplands: a new high resolution map derived from remote sensing, crop inventories and climate data. *Int. J. Appl. Earth Obs. Geoinf.* 38, 321–334. <https://doi.org/10.1016/j.jag.2015.01.014>.
- Scipal, K., Dorigo, W., de Jeu, R., 2010. Triple collocation – A new tool to determine the error structure of global soil moisture products. In: 2010 IEEE International Geoscience and Remote Sensing Symposium. Presented at the IGARSS 2010–2010 IEEE International Geoscience and Remote Sensing Symposium. IEEE, Honolulu, HI, USA, pp. 4426–4429. <https://doi.org/10.1109/IGARSS.2010.5652128>.
- Seneviratne, S.I., Corti, T., Davin, E.L., Hirschi, M., Jaeger, E.B., Lehner, I., Orlowsky, B., Teuling, A.J., 2010. Investigating soil moisture–climate interactions in a changing climate: a review. *Earth Sci. Rev.* 99, 125–161. <https://doi.org/10.1016/j.earscirev.2010.02.004>.
- Siebert, S., Döll, P., Hoogeveen, J., Faures, J.M., Frenken, K., Feick, S., 2005. Development and validation of the global map of irrigation areas. *Hydrol. Earth Syst. Sci. Discuss.* 2 (4), 1299–1327. <https://doi.org/10.5194/hess-9-535-2005>.
- Siebert, S., Henrich, V., Frenken, K., Burke, J., 2013. Update of the Digital Global Map of Irrigation Areas to Version 5. 171.
- Stoffelen, A., 1998. Toward the true near-surface wind speed: error modeling and calibration using triple collocation. *J. Geophys. Res.* 103, 7755–7766. <https://doi.org/10.1029/97JC03180>.
- Su, C.-H., Ryu, D., Crow, W.T., Western, A.W., 2014a. Stand-alone error characterisation of microwave satellite soil moisture using a Fourier method. *Remote Sens. Environ.* 154, 115–126. <https://doi.org/10.1016/j.rse.2014.08.014>.
- Su, C.-H., Ryu, D., Crow, W.T., Western, A.W., 2014b. Beyond triple collocation: applications to soil moisture monitoring: beyond triple collocation. *J. Geophys. Res. Atmos.* 119, 6419–6439. <https://doi.org/10.1002/2013JD021043>.
- Thenkabail, P.S., Biradar, C.M., Noojipady, P., Dheeravath, V., Li, Y., Velpuri, M., Gumma, M., Gangalkunta, O.R.P., Turrall, H., Cai, X., Vithanage, J., Schull, M.A., Dutta, R., 2009. Global irrigated area map (GIAM), derived from remote sensing, for the end of the last millennium. *Int. J. Remote Sens.* 30, 3679–3733. <https://doi.org/10.1080/01431160802698919>.
- Tuinenburg, O.A., de Vries, J.P.R., 2017. Irrigation patterns resemble ERA-interim reanalysis soil moisture additions: IRRIGATION EFFECTS IN ERA-INTERIM. *Geophys. Res. Lett.* 44, 10,341–10,348. <https://doi.org/10.1002/2017GL074884>.
- Wagner, W., Lemoine, G., Rott, H., 1999. A method for estimating soil Moisture from ERS scatterometer and soil data. *Remote Sens. Environ.* 70, 191–207. [https://doi.org/10.1016/S0030-4257\(99\)00036-X](https://doi.org/10.1016/S0030-4257(99)00036-X).
- Wagner, W., Hahn, S., Kidd, R., Melzer, T., Bartalis, Z., Hasenauer, S., Figa-Saldana, J., de Rosnay, P., Jann, A., Schneider, S., Komma, J., Kubu, G., Brugger, K., Aubrecht, C., Züger, J., Gangkofner, U., Kienberger, S., Brocca, L., Wang, Y., Blöschl, G., Eitzinger, J., Steinnocher, K., 2013. The ASCAT soil moisture product: a review of its specifications, validation results, and emerging applications. *Meteorol. Z.* 22, 5–33. <https://doi.org/10.1127/0941-2948/2013/0399>.
- Werth, D., Avissar, R., 2004. The regional evapotranspiration of the Amazon. *J. Hydrometeorol.* 5, 10.
- Wigneron, J.-P., Ferrazzoli, P., Calvet, J.-C., Bertuzzi, P., 1999a. A parametric study on passive and active microwave observations over a soybean crop. *IEEE Trans. Geosci. Remote Sens.* 37, 2728–2733. <https://doi.org/10.1109/36.803421>.
- Wigneron, J.-P., Ferrazzoli, P., Olioso, A., Bertuzzi, P., Chanzy, A., 1999b. A simple approach to monitor crop biomass from C-band radar data. *Remote Sens. Environ.* 69, 179–188. [https://doi.org/10.1016/S0034-4257\(99\)00011-5](https://doi.org/10.1016/S0034-4257(99)00011-5).
- Wigneron, J.-P., Jackson, T.J., O'Neill, P., De Lannoy, G., de Rosnay, P., Walker, J.P., Ferrazzoli, P., Mironov, V., Bircher, S., Grant, J.P., Kurum, M., Schwank, M., Munoz-Sabater, J., Das, N., Royer, A., Al-Yaari, A., Al Bitar, A., Fernandez-Moran, R., Lawrence, H., Mialon, A., Parrens, M., Richaume, P., Delwart, S., Kerr, Y., 2017. Modelling the passive microwave signature from land surfaces: a review of recent results and application to the L-band SMOS & SMAP soil moisture retrieval algorithms. *Remote Sens. Environ.* 192, 238–262. <https://doi.org/10.1016/j.rse.2017.01.024>.
- Wu, X., Xiao, Q., Wen, J., You, D., 2019. Direct comparison and triple collocation: which is more reliable in the validation of coarse-scale satellite surface albedo products. *J. Geophys. Res. Atmos.* 124, 5198–5213. <https://doi.org/10.1029/2018JD029937>.
- Ulaby, F.T., Long, D.G., Blackwell, W.J., Elachi, C., Fung, A.K., Ruf, C., 2014. *Microwave radar and radiometric remote sensing* (vol. 4, no. 5). University of Michigan Press, Ann Arbor, MI, pp. 321–329.
- Yilmaz, M.T., Crow, W.T., 2014. Evaluation of assumptions in soil moisture triple collocation analysis. *J. Hydrometeorol.* 15, 1293–1302. <https://doi.org/10.1175/JHM-D-13-0158.1>.
- Zohaib, M., Kim, H., Choi, M., 2019. Detecting global irrigated areas by using satellite and reanalysis products. *Sci. Total Environ.* 677, 679–691. <https://doi.org/10.1016/j.scitotenv.2019.04.365>.